Chemical Geology 644 (2024) 121865

Contents lists available at ScienceDirect

Chemical Geology

journal homepage: www.elsevier.com/locate/chemgeo

Trace elements (REE + Y) reveal marine, subaerial, and hydrothermal controls on an early Archean habitat for life: The 3.48 Ga volcanic-caldera system of the dresser formation, Pilbara Craton

T. Djokic [a,b,*], R. Bolhar [c], L.A. Brengman [d], J.R. Havig [e,f], M.J. Van Kranendonk [a,g]

[a] Australian Centre for Astrobiology, School of Biological Earth and Environmental Sciences, University of New South Wales, New South Wales 2052, Australia
[b] Australian Museum Research Institute, Sydney, New South Wales, Australia
[c] School of Geosciences, University of the Witwatersrand, Johannesburg 2000, South Africa
[d] Department of Earth and Environmental Sciences, University of Minnesota - Duluth, Duluth, MN 55812, USA
[e] Department of Plant and Microbial Biology, University of Minnesota – Twin Cities, Saint Paul, MN 55108, USA
[f] Department of Earth and Environmental Sciences, University of Minnesota – Twin Cities, Minneapolis, MN 55455, USA
[g] Big Questions Institute, University of New South Wales Australia, Kensington, New South Wales, Australia

ARTICLE INFO

Editor: Marco Fiorentini

ABSTRACT

Host to some of Earth's earliest evidence of life, the fossiliferous lowermost chert-barite sequence (DFc1) in the ~3.5 Ga Dresser Formation of the Pilbara Craton, Western Australia is interpreted to have deposited within a dynamic volcanic-hydrothermal caldera. To date, three end-member fluid compositions (marine, hydrothermal, and subaerial) have been identified using trace and rare earth elements. However, this data has been limited to a few, single rock units, providing only snapshots at various depositional time intervals, and does not represent a synthesis of habitat evolution over time. Here, we present a systematic trace and rare earth element study of 31 whole-rock samples from 10 lithofacies across the entire stratigraphic sequence. Samples include bedded cherts (silicified chemical and clastic sedimentary rocks), hot spring geyserite and sinter terracettes, jaspilitic chert, and silicified volcaniclastic siltstone. Four lithostratrigraphically-defined assemblages (A1-A4) in DFc1 illustrate a transition from marine (underlying pillowed North Star Basalts, deep marine cherts) to shallow water and subaerial conditions (evaporitic carbonate-chert couplets, hot spring geyserite and sinter terracettes, channelized conglomerates and basaltic-evolved volcaniclastics)(A1-A2), followed by a return to deep marine conditions (jaspilitic chert, volcaniclastic siltstone and sandstone)(A3-A4). Our trace and rare earth element data enhance the four-stage model (reflecting, A1-A4 respectively) as follows: stages 1–2, crustal inflation generated the emplacement of a deep-rooted magmatic chamber, leading to surface uplift and a transition from deep water to hydrothermally-influenced semi-restricted lakes, stromatolites, and subaerial hot springs. Trace and rare earth element patterns of A2 geyserite indicate the circulation of low-temperature near-surface, non-marine geothermal fluids through basaltic to more evolved volcaniclastic rocks. REE + Y patterns of sinter terracettes may indicate the formation of hot spring travertine in DFc1; stages 3–4, hydrothermally-influenced jaspilites and volcaniclastic sediments deposited in marine basins driven by caldera collapse. This stifled stromatolite growth and represents the end of subaerial exposure. This work contributes to ongoing efforts to reconstruct Earth's early life habitats, which inform the search for life on Mars and origin of life studies.

1. Introduction

Host to some of Earth's earliest evidence of life, the lower chert-barite sequence in the ~3.5 Ga Dresser Formation (DFc1) of the North Pole Dome, Pilbara Craton, Western Australia is a globally significant unit (Walter et al., 1980; Buick and Dunlop, 1990; Nijman et al., 1998; Van Kranendonk, 2006; Van Kranendonk et al., 2008; Djokic and Van Kranendonk, 2018; Baumgartner et al., 2020b; Baumgartner et al., 2020c; Djokic et al., 2021). It provides a rare glimpse of an early Archean habitat, informing the search for ancient life on Mars (e.g., Van

* Corresponding author at: Australian Centre for Astrobiology, School of Biological Earth and Environmental Sciences, University of New South Wales, New South Wales 2052, Australia.
E-mail address: tara.djokic@australian.museum (T. Djokic).

https://doi.org/10.1016/j.chemgeo.2023.121865
Received 12 September 2023; Received in revised form 20 November 2023; Accepted 24 November 2023
Available online 1 December 2023
0009-2541/© 2023 Elsevier B.V. All rights reserved.

Kranendonk et al., 2021b) and origin of life studies (e.g., Van Kranendonk et al., 2021a). Inferred biosignatures, including stromatolites, are interpreted to have formed under either passive marginal marine (e.g., Buick and Dunlop, 1990; Noffke et al., 2013; Hickman-Lewis et al., 2022) or active volcanic-hydrothermal conditions (Nijman et al., 1998; Van Kranendonk et al., 2008; Harris et al., 2009; Djokic et al., 2021). Given the significance of DFc1, resolving this debate remains important.

Palaeoenvironmental models of DFc1 are based on lithostratigraphic data, enhanced by isotopic, trace element, and REE + Y geochemistry (Bolhar et al., 2004; Lindsay et al., 2005; Van Kranendonk et al., 2019; Djokic et al., 2021). Extensive mapping, sedimentological, and petrographic studies of DFc1 document biosignatures within a complex sequence of metasedimentary units (chemical and clastic), crosscut by large chert-barite veins (Buick and Dunlop, 1990; Nijman et al., 1998; Van Kranendonk et al., 2008; Tadbiri and Van Kranendonk, 2020; Djokic et al., 2021). Emplacement of these veins led to extensive hydrothermal alteration of footwall basalts, widespread silicification and replacement of primary sedimentary units, and discordant and concordant chert and barite veining within those sediments (Buick and Barnes, 1984; Van Kranendonk, 2006). This has complicated the local lithology, making palaeoenvironmental reconstructions challenging.

Original studies suggested DFc1 formed in a passive, shallow-water, marginal marine evaporite-dominated lagoon similar to Shark Bay, Western Australia (Barley et al., 1979; Walter et al., 1980; Groves et al., 1981; Buick and Dunlop, 1990). In this model, hydrothermal veins were interpreted as post-depositional, causing late-stage baritisation and/or silicification of precursor evaporitic gypsum beds (now barite), gypsum- and carbonate-bearing mudstones and sandstones (now silicified), volcaniclastic rocks, pebble conglomerates, desiccated intraclast conglomerates (now silicified), and stromatolites (Buick and Dunlop, 1990).

Subsequent investigators revised the marginal marine model, documenting syngenetic hydrothermal activity and active growth faulting within a dynamic, low eruptive piecemeal-type volcanic caldera setting as follows:

1) rapid lateral and temporal (stratigraphic) facies changes across active synsedimentary growth faults filled by hydrothermal chert and barite (Nijman et al., 1998; Van Kranendonk et al., 2008; Djokic et al., 2021)
2) syngenetic hydrothermal vents (chert-barite veins) passing vertically through, and branching laterally into bedded sediments (Nijman et al., 1998; Van Kranendonk and Pirajno, 2004; Van Kranendonk, 2006; Van Kranendonk et al., 2008; Harris et al., 2009; Tadbiri and Van Kranendonk, 2020; Caruso et al., 2021)
3) a boxwork swarm of chert-barite veins (with disseminated pyrite and organic matter) that extend 2 km down-section into underlying, hydrothermally altered North Star Basalts. The veins are restricted below the uppermost chert in the Dresser Formation, transitioning from fine-grained black silica (chert) in the lower, deeper parts to barite and epithermal quartz in the upper 70 m, near-surface parts of veins that penetrate the sedimentary sequence (Nijman et al., 1998; Van Kranendonk and Pirajno, 2004; Van Kranendonk et al., 2008)
4) advanced argillic alteration restricted to the immediate footwall pillow basalts (North Star Basalt) of DFc1 indicates a *syn*-depositional epithermal-hydrothermal system (Van Kranendonk and Pirajno, 2004; Caruso et al., 2021)
5) the presence of eroded hydrothermal material within sandstone and conglomerate in upper DFc1 sedimentary horizons (Van Kranendonk, 2006; Van Kranendonk et al., 2008)
6) structural and kinematic analysis identified four vein sets relating to emplacement during repeated pulses of magma-driven surface uplift and subsidence of a piecemeal-type volcanic caldera largely during (sets 1–3), and post-dating (set 4), sediment deposition (Poole, 2013; Tadbiri and Van Kranendonk, 2020). These veins caused zoned, epithermal-type hydrothermal alteration of the footwall basaltic rocks (Van Kranendonk and Pirajno, 2004; Harris et al., 2009; Caruso et al., 2021)
7) hot spring geyserite and sinter terracettes widely distributed across DFc1 (Djokic et al., 2017; Djokic et al., 2021) and fluid inclusions from epithermal quartz veins indicate near neutral alkali-chloride hot spring fluid circulation (Harris et al., 2009)

In this model, the evolution of a volcanic caldera is thought to have generated growth fault networks that acted as conduits for hydrothermal fluid circulation during deposition of the stromatolite-bearing sedimentary units. Multiple episodes of hydrothermal circulation precipitated primary hydrothermal barite and chert as cross-cutting and bedding-parallel veins into the subsurface of an at least temporally emerged landscape and/or coastline that fed microbially-inhabited subaerial hot springs (Djokic et al., 2021; Van Kranendonk et al., 2021a).

What remains a subject of discussion is the relationship between stromatolite formation and the Dresser volcanic-hydrothermal system. Alternative models based on limited sampling (Noffke et al., 2013) and a lack of discrimination between primary and secondary siliceous units, and stromatolitic cherts (Hickman-Lewis et al., 2022) maintain that stromatolites formed under passive marginal marine conditions despite acknowledging strong evidence for hydrothermal components. This highlights the need for continued investigation of the various hydrothermal, marine, and terrestrial conditions that hosted life in DFc1.

To date, a few selected chemical sedimentary units in DFc1 have been geochemically linked to three end-member fluid compositions – marine, hydrothermal, and terrestrial (and any combinations), in addition to variable clastic input. This has been limited to subaerial hot spring geyserite (Djokic et al., 2021), cm-bedded evaporitic carbonate-chert couplets (Van Kranendonk et al., 2003; Van Kranendonk et al., 2019), bedded jaspilitic chert (Johnson et al., 2022a; Johnson et al., 2022b), and stromatolitic chert (Hickman-Lewis et al., 2022). Additionally, many other silicified units of DFc1 have not been geochemically investigated. This has resulted in a limited set of geochemical snapshots across various depositional time intervals that do not represent a synthesis of the evolution of the DFc1 system.

Here, we provide a systematic trace and rare earth element + yttrium (REE + Y) investigation of the entire DFc1 system, based on 31 whole-rock samples from 10 lithostratigraphically-defined lithofacies across the entire stratigraphy. This study aims to: 1) determine protoliths of undefined silicified sedimentary units; 2) contextualise subaerial hot spring units; 3) define the compositions of the bedrock that interacted with geothermal fluids; and 4) refine the depositional setting and geological history of DFc1. Implicit in these aims is to delineate between primary and secondary REE + Y signatures and develop a holistic understanding of the context of the DFc1 system that led to stromatolite genesis. This work contributes to the ongoing efforts to reconstruct Earth's early life habitats and support astrobiological research.

1.1. Geological setting

The ca. 3.48 Ga Dresser Formation of the North Pole Dome, Pilbara Craton, Western Australia is very well-preserved for its age (Fig. 1A) (Thorpe, 1992; Van Kranendonk, 2000; Van Kranendonk, 2006; Hickman and Van Kranendonk, 2012), having only experienced lower greenschist facies metamorphism and no penetrative strain (Van Kranendonk and Pirajno, 2004; Van Kranendonk et al., 2008; Caruso et al., 2021). Formally, it comprises two relatively thin (10's to 100's m) sedimentary sequences (though five are documented) of silicified sedimentary rocks (cherts), separated by up to 2 km-thick units of doleritic and pillowed komatiitic basalt (Nijman et al., 1998; Van Kranendonk, 2000; Van Kranendonk, 2006; Van Kranendonk et al., 2007; Van Kranendonk et al., 2008). The uppermost chert unit comprises millimetre to centimetre bedded grey-white-black chert and jasper, which is locally split by post-depositional dolerite sills (Van Kranendonk et al., 2019). The lowermost chert unit is the fossiliferous chert-barite sequence

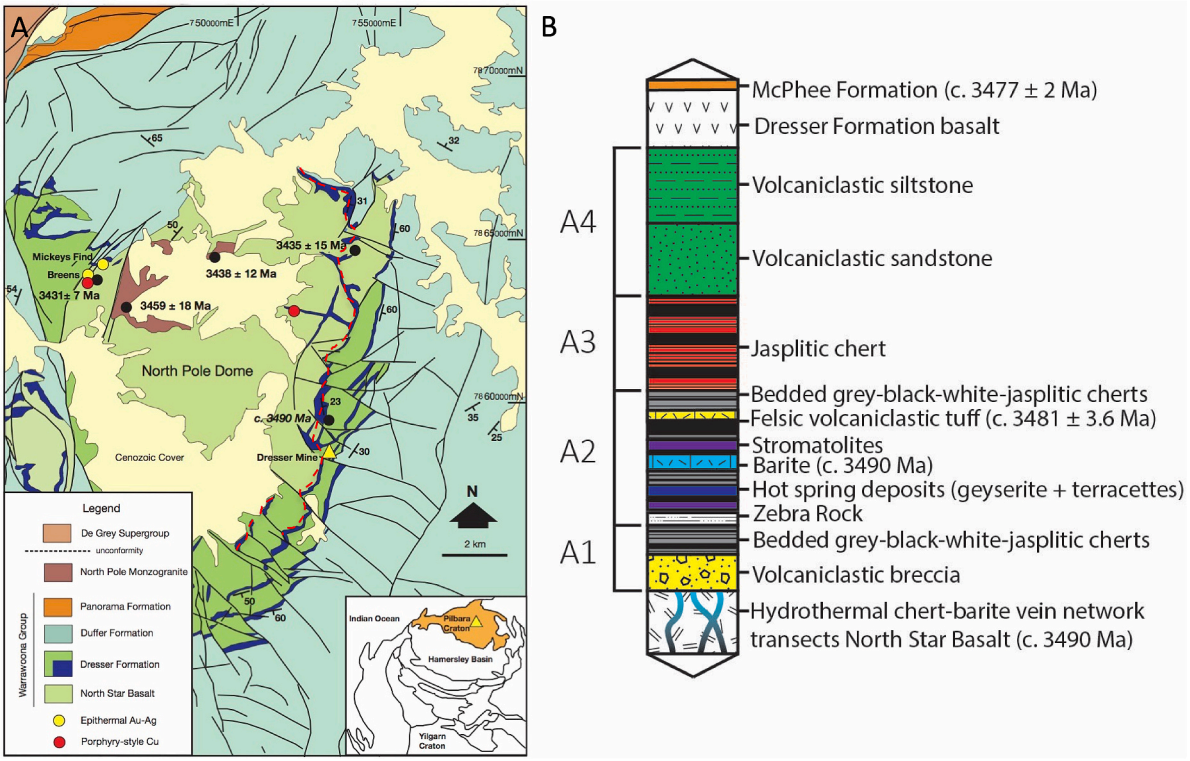


Fig. 1. Location and stratigraphy of the Dresser Formation lower chert-barite sequence. (A) Geological map of the Dresser Formation (modified from Harris et al., 2009). Dashed red line - Dresser Formation lower chert-barite sequence (DFc1). (B) Generalized stratigraphy of the four assemblages comprising DFc1; A1 - a variety of cherty metasediments, volcaniclastic conglomerate ± stromatolites; A2 - a variety of grey-black-white-jaspilitic cherts, carbonate-chert couplets with evaporative aragonite rosette casts ('zebra rock'), volcaniclastics, and hot spring geyserite and terracettes linked with a variety of biosignatures; A3 - jaspilitic chert, and; A4 - fine to coarse-grained green, basaltic volcaniclastics. Composite age data from Thorpe (1992), Van Kranendonk (2006), and Van Kranendonk et al. (2002, 2008) . (For interpretation of the references to colour in this figure legend, the reader is referred to the web version of this article.)

(hereafter, DFc1), formally termed the North Pole Chert Member. Well-documented to contain various biosignatures including stromatolites (see Section 1.2), DFc1 is the focus of this study.

DFc1 is 1 – 288 m-thick, composed of metasedimentary units cross-cut by a network of syngenetic hydrothermal chert-barite veins (Nijman et al., 1998; Van Kranendonk et al., 2019). Four distinct lithostratigraphic assemblages (A1-A4) are inferred to reflect the evolution of a low-eruptive, volcanic-hydrothermal caldera setting (Van Kranendonk et al., 2019; Djokic et al., 2021). A1 contains cherty metasedimentary rocks including localized jaspilitic chert interpreted as a restricted terrestrial basin (Johnson et al., 2022a; Johnson et al., 2022b), felsic volcaniclastic conglomerate-sandstone-siltstone, and minor stromatolitic clasts in volcanic breccia. A2 contains grey-black-white-jaspilitic chert, carbonate-chert couplets with evaporative aragonite crystal casts (Van Kranendonk et al., 2003; Van Kranendonk et al., 2008; Otálora et al., 2018), volcaniclastic rocks, stromatolites displaying sulfidized and non-sulfidized compositions, and hot spring geyserite and terracettes linked with a variety of biosignatures. A3 contains deep marine jaspilitic chert (Johnson et al., 2022a; Johnson et al., 2022b). A4 consists of basaltic volcaniclastic sandstone and siltstone and local lenses of deep marine jaspilitic chert.

1.2. Biosignature preservation

Compared to sites of similar age, DFc1 has good exposure and diversity of interpreted biosignatures. Stromatolite forms include domical, conical, wrinkly or wavy, stratiform, nodular, and columnar (Walter et al., 1980; Buick and Dunlop, 1990; Nijman et al., 1998; Van Kranendonk, 2011; Djokic et al., 2021). The independent growth of these structures with respect to shallow water sedimentation and resemblance to younger stromatolites supports their biogenic origin (Walter et al., 1980; Van Kranendonk, 2006; Van Kranendonk, 2011; Van Kranendonk et al., 2019). Biological activity is also supported by microtextural, geochemical, and isotopic data. Sulfidized (pyrite) stromatolites from unweathered drillcore preserve organic matter (OM) strands and filaments, and a carbon isotopic signature indicative of biological matter ($\delta^{13}C_{OM} = -29.6‰ \pm 0.3‰$) (Baumgartner et al., 2019). They also preserve cyclic concentrations of transition metals and metalloids that are known to bind to OM and are indicative of biochemical processes (Baumgartner et al., 2020c). Putative carbonaceous microfossils, many showing $\delta^{13}C_{OM}$ values indicative of biological fractionation, are observed within both bedded chert and hydrothermal chert veins (Dunlop et al., 1978; Ueno et al., 2001a; Ueno et al., 2001b; Ueno et al., 2004; Glikson et al., 2008; Morag et al., 2016). Methane in fluid inclusions from *syn*-depositional hydrothermal veins is used to argue for methanogenesis (Ueno et al., 2006). Kerogen from hydrothermal veins displays $\delta^{13}C_{TOC}$ (-32.8 ± 0.3 ‰) and stable carbon isotopic compositions (-29.4 to -33.3 ‰) of short-chain *n*-alkanes, which together indicate biological organic matter (Duda et al., 2018). Multiple sulfur isotope analyses (ΔS^{33} and δS^{32}) from barite (sulfate) and disseminated microscopic pyrite (sulfide) indicate either microbial cycling of elemental sulfur and/or microbial sulfate reduction (Shen et al., 2001; Philippot et al., 2007; Shen et al., 2009; Baumgartner et al., 2020a).

Of course, researchers have long questioned biological evidence of this antiquity. For example, stromatolites are suggested as abiogenic crusts (Lowe, 1994; McLoughlin et al., 2008). Microfossils are suggested as mineral artifacts or volcanic glass vesicles (Brasier et al., 2002, 2015, Wacey et al., 2015, 2018). Negative $\delta^{13}C$ values are considered the product of abiological Fischer-Tropsch-Type (FTT) synthesis (Brasier et al., 2004; van Zuilen, 2019). Alternative abiogenic origins for sulfur isotopic fractionation include photochemical reactions (Muller et al., 2016; Liu et al., 2021) or hydrothermal fluid circulation through

sediment – though the micro-scale heterogeneity of sulfur isotopes is noted as more consistent with sulfate-reducing bacteria (Wacey et al., 2015). Despite the abiological alternatives, the sheer volume and diversity of inferred biosignatures in DFc1 strongly supports its prior existence.

2. Origin of REE + Y in chemical sedimentary rocks

Trace and rare earth element analysis can define depositional conditions of Archean chemical sedimentary rocks (Van Kranendonk et al., 2003; Bolhar et al., 2005; Allwood et al., 2010). They are effective in discriminating between various types of chemical precipitates because they fractionate differently as a group under distinct physicochemical conditions (Cox et al., 1984; Kim et al., 1991; Bolhar et al., 2004; Johannesson et al., 2005). They can indicate primary fluid compositions (e.g., marine and hydrothermal) (Van Kranendonk et al., 2003; Bolhar et al., 2004; Bolhar et al., 2005; Allwood et al., 2010; Uysal et al., 2011; Bolhar et al., 2015; Hamilton et al., 2019a) and reveal the precursor composition of altered volcanic rocks and volcaniclastic input (Van Kranendonk et al., 2003; Brengman and Fedo, 2018). This is important for identifying silicified or post-depositionally altered seawater and non-seawater deposits and fingerprinting continental, mantle, and hydrothermal input (Elderfield, 1988; Lewis et al., 1998; Kamber et al., 2005; Brengman and Fedo, 2018).

Chemically precipitated rocks form from seawater or freshwater, as carbonates or sulfates (referred to as hydrogenous sediments), but also form hydrothermal deposits including submarine chimney vents, bedded cherts, subaerial sinter, and hydrothermal veins (Buick and Dunlop, 1990; Allwood et al., 2010; Uysal et al., 2011; Hofmann et al., 2013; Feng et al., 2014; Dekov et al., 2015). Below we provide a summary of REE + Y characteristics in marine versus hydrothermal precipitates.

2.1. Marine versus hydrothermal precipitates

Modern and ancient marine carbonates can reliably record REE + Y compositions that reflect conditions and processes at the time of precipitation (Webb and Kamber, 2000; Kamber and Webb, 2001). REE + Y in marine precipitates are influenced by terrestrial weathering, hydrothermal input, and particle-solution interactions – such as particle scavenging that removes REEs from solution (De Baar et al., 1985) – related to salinity, water depth, and redox (Goldberg, 1954; Elderfield, 1988; Piepgras and Jacobsen, 1992; Bertram and Elderfield, 1993; Greaves et al., 1999). When normalized to crustal proxies i.e., estimates

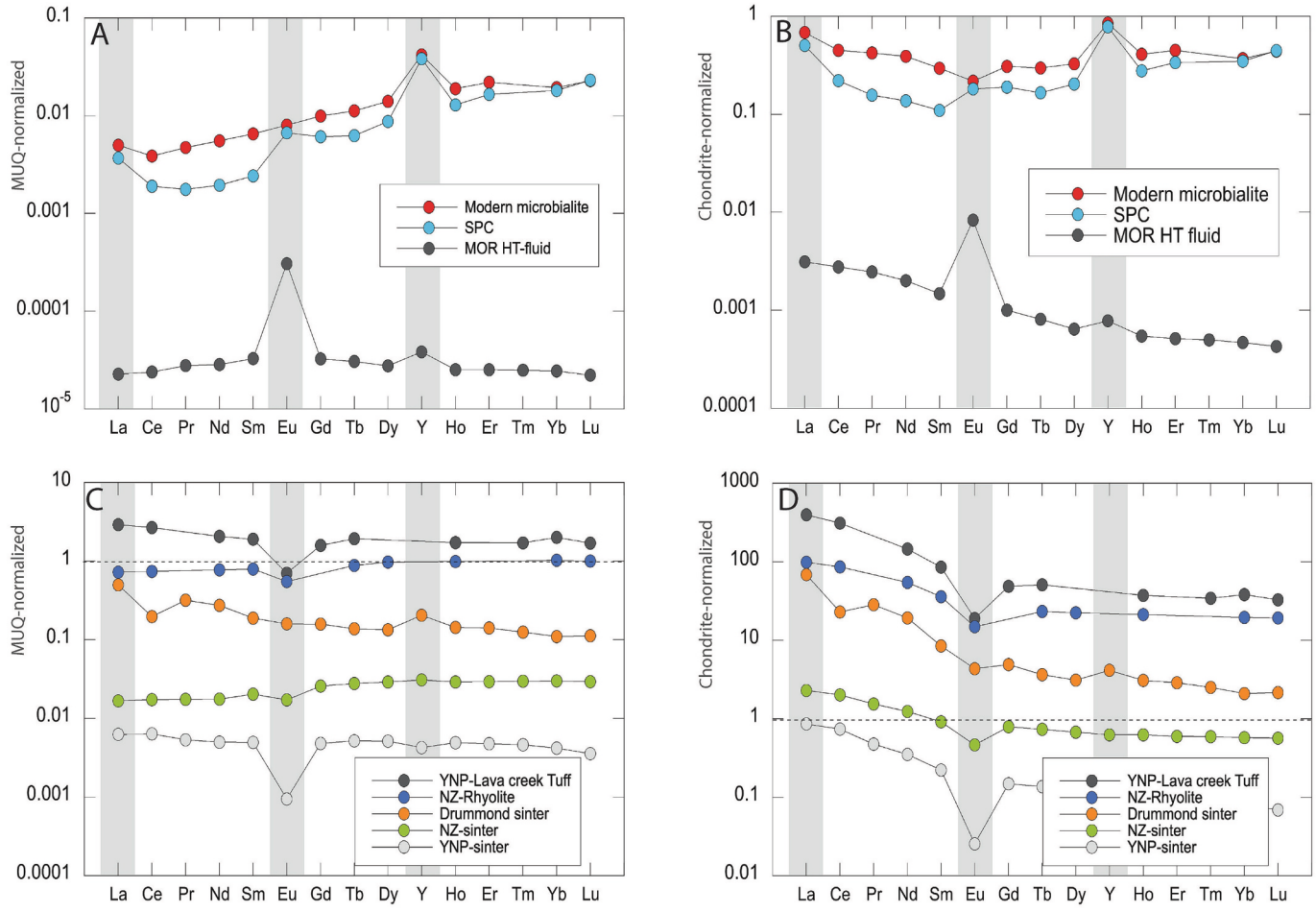


Fig. 2. REE + Y patterns of seawater versus hydrothermal precipitates. (A-B) MUQ- and chondrite-normalized REE + Y of a modern seawater carbonate (Modern microbialite) from Heron Island (Webb and Kamber, 2000: Table 1, sample H-1 m), Archean stromatolitic carbonate (SPC) from the c. 3.43 Ga Strelley Pool Formation (Van Kranendonk et al., 2003: Table 1, sample 177,882–1/4), and high temperature (>300 °C) mid-ocean ridge hydrothermal fluid (MOR HT-fluid) from 17 to 19°S, East Pacific Rise (Douville et al., 1999: Table 3, sample ND17G2, Mg-free end-member). (C-D) MUQ- and chondrite-normalized REE + Y of Phanerozoic subaerial sinters and their igneous host rocks, where available. New Zealand (NZ-sinter) sinter against unaltered rhyolite (NZ-Rhyolite) from the Taupo Volcanic Zone (Hopf, 1993: Table 3, sample 1). Yellowstone National Park, USA, sinter (YNP-sinter) against rhyolite (YNP-Rhyolite) from the 'Lava Creek tuff' Member (Christiansen, 2001: Table 14, sample 74Y-180B). Drummond Basin sinter sample (Drummond sinter). Phanerozoic sinter sample plot data from Djokic et al. (2021): Supp. Table S1, samples TD16-UMA-SINTER, LGB-SC-4-18, and 28.2/6/92.

of REE + Y in average continental crust represented by shale – PAAS or MUQ (McLennan, 1989; Kamber et al., 2005), the REE + Y of modern seawater precipitates are characterized by the following (Fig. 2A-B) (Webb and Kamber, 2000):

- Depletion of light-mid REE (LREE – MREE) relative to heavy REE (HREE) (Lee and Byrne, 1992; Sholkovitz et al., 1994)
- A positive lanthanum (La) anomaly (Bau and Dulski, 1996)
- Small gadolinium (Gd) and erbium (Er) anomalies (Alibert and McCulloch, 1993; Bau and Dulski, 1996)
- A strong positive yttrium (Y) anomaly (Bau, 1996; Nozaki et al., 1997)
- A negative Ce anomaly (typical of oxic conditions) (Tostevin et al., 2016)

Ancient carbonates also display these REE + Y features but lack Ce anomalies and exhibit positive europium (Eu) anomalies due to anoxic, hydrothermal conditions inferred during the Archean. For an extended review of the origin of these REE + Y characteristics see Supp. Data 1.

In contrast, the REE + Y composition of hydrothermal precipitates (submarine and subaerial sinters) reflect the igneous host rocks through which the hydrothermal fluids circulated (Fig. 2C-D) (Sveinbjornsdottir et al., 1986; Lewis et al., 1997; Lewis et al., 1998; Douville et al., 1999; McCarthy et al., 2005; Wood, 2006; Bao et al., 2008; Dekov et al., 2015). Submarine hydrothermal deposits reflect the interaction of seawater with oceanic basaltic crust and high-temperature (>300^{o} C) hydrothermal fluids (Douville et al., 1999; Dekov et al., 2015). This results in basaltic igneous REE + Y patterns with inherited seawater features, such as Y anomalies (Douville et al., 1999; Dekov et al., 2015), and strongly positive Eu anomalies (Mills and Elderfield, 1995). Subaerial sinters are derived from meteoric water interaction with continental felsic rocks with/without input from the magma chamber. These display relatively flat shale-normalized patterns, and enriched LREE when chondrite-normalized (Fig. 2C-D) (Lewis et al., 1997; Douville et al., 1999; Feng et al., 2014). These lower temperature (<250 °C) subaerial sinters typically lack positive Y and Eu anomalies (Hopf, 1993; Wood, 2006; Uysal et al., 2011; Djokic et al., 2021: Supp. Fig. 7).

3. Methods

3.1. Mapping, sample collection and petrography

Thirty-one samples were collected during mapping in 2016–2018 of 100 measured stratigraphic sections from the 14 km-long eastern exposure of DFc1 (Djokic et al., 2021: Supp. Fig. 2). Several samples were collected from laterally and temporally distinct locations to test the reproducibility of trace element patterns across the studied lithofacies. Polished and standard thin sections (30 μm-thick) were prepared for each of the lithofacies studied by Australian Petrographics PTY LTD and examined using a Nikon Eclipse Ci POL optical light microscope with a Nikon DS-Vi1 camera.

3.2. Trace element geochemistry

Trace element concentrations were measured using Inductively Coupled Plasma-Mass Spectrometry (ICP-MS) at the School of Earth Sciences, University of Melbourne. Subsamples were extracted from the centre of selected hand samples using a diamond-tipped rock saw to avoid surface contamination encountered during transport and storage. Samples were either lightly crushed, or in the case of the sinter/geyserite samples, milled to a powder using a Retches Mixer mill with agate ball mills. The agate mill was cleaned between each sample by powdering a small amount of the subsequent sample, which was then blow out with an air gun before the mill was cleaned with ethanol and dried. Between 140 and 470 mg of samples (25 mg for sinter/geyserite samples) were digested with an HF-HNO_3 (2:1) mixture (4 x Teflon distilled Merck analytical reagent grade HF and 2 x quartz distilled Univar analytical reagent HNO_3) in capped Teflon vials on a hotplate overnight at 135 °C, then evaporated to dryness, refluxed twice with concentrated HNO_3, then dissolved overnight in dilute HNO_3. Double quartz distilled Univar analytical reagent HNO_3 was used. Solutions were transferred to transparent polycarbonate tubes and diluted with 18.2 MΩ/cm deionized water. An aliquot of each solution was further diluted with HNO_3 solution containing an internal standard mixture to give total dilution factors including ca. 100 and 3500. Note that the lower 1:100 dilution factor was reserved for Si-rich materials (chert/quartz) to improve detection limits, while ca. 3500× was used for non-Si-rich samples (Baldwin et al., 2011). The procedure was based on a visual estimate of the mass of solids that remained after digestion, informed by previous experience digesting similar rock types (e.g., Van Kranendonk et al., 2003). Analytical and drift correction procedures are comprehensively described in Eggins et al. (1997), and summarised below:

The method uses a natural rock standard for calibration, internal drift correction using multi-internal standards (Li^{6}, Sr^{84}, ^{103}Rh, ^{187}Re, and U^{235}), external drift monitors, and aggressive washout procedures. Differences in the methods of this study from Eggins et al. (1997) were applied as follows: 1) ^{147}Sm, ^{169}Tm, ^{115}In, and ^{209}Bi were not used as internal standards as these are analytes; and (2) two digestions of the USGS standard W-2 were used for instrument calibration. The preferred concentrations of W-2 were mostly derived by analyzing it against synthetic standards and a literature survey of isotope dilution analyses (Kamber et al., 2003; Kamber et al., 2005; Babechuk et al., 2010). Long-term reproducibility data was captured for BHVO-2 as an unknown yielding relative standard deviation (%RSD) between 0 and 2% for elements investigated in this study (Supp. Table 2).

Samples were analyzed on an Agilent 7700× ICP-MS, tuned to give barium oxide levels of 0.067%. Four replicates of 100 scans per replicate were measured for each isotope. Long sample wash-out times of 6 min with solutions of 0.5% Triton X-100, 0.025% HF in 5% HNO_3, and 2% HNO_3, and long sample uptake times of 120 s were applied. Samples with Ba/Eu ratios >4000 were reanalyzed for REE and Y under conditions with a Ba oxide level of 0.019% using dilution gas mode and He mode with a 2 ml/min He flow to the collision cell.

In this study, analyses of La, Ce, Gd, Y, and Eu anomalies are measured as follows (Murray et al., 1991; Bau, 1996; Bolhar et al., 2004; Kamber et al., 2005):

1. Positive La anomalies as $La/La^{*} = La/(3Pr - 2Nd) > 1$
2. Negative Ce anomalies as $Ce/Ce^{*} = Ce/(2Pr\text{-}1Nd) < 1$
3. Gd anomalies are calculated using $Gd/Gd^{*} = Gd/(2\,Tb - 1Dy)$ relative to 1, where >1 is positive, and < 1 is negative
4. Y anomalies are based on Y/Ho ratios relative to chondritic values of ~26. Igneous rocks typically display ratios between ~24–34, whereas marine precipitates are strongly super-chondritic, with high Y/Ho ratios of ~40–90
5. Positive Eu anomalies are calculated from $Eu/Eu^{*} = Eu/(0.5Sm + 0.5Gd) > 1$

REE + Y analysis are presented in both Mud of Queensland (MuQ)- and chondrite-normalized plots based on the rationale that lithofacies in DFc1 have varying input from clastic detritus, the influence of two or more end-member fluids (marine/terrestrial ± hydrothermal), and an influence from footwall volcanic rocks during hydrothermal fluid circulation. For extended method details regarding normalisation, possible Eu errors, and data comparison considerations see Supp. Data 1.

4. Results

We present trace and rare earth elements (REE + Y) in 31 whole-rock samples from 10 DFc1 lithofacies (Figs. 3–10). These include a variety of "cherts" (senso lato) defined as fine-grained silicified chemical and clastic sedimentary rocks with poorly preserved precursor sediments

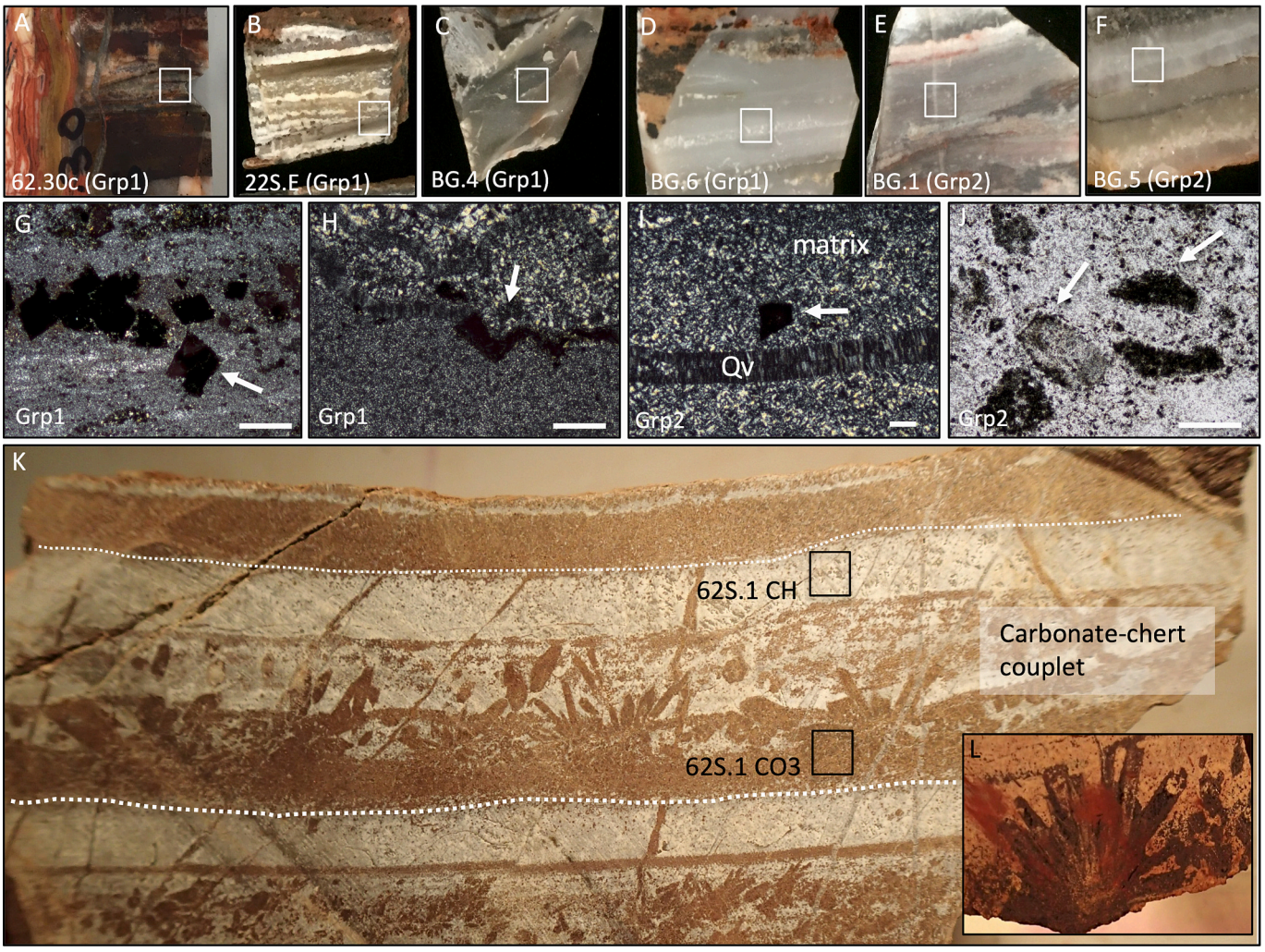


Fig. 3. DFc1 bedded grey-black-white chert and carbonate-chert couplets. (A-J) Bedded grey-black-white chert samples. Six samples display two groups distinguished by their REE + Y patterns. (A-D) Group 1 hand sample photographs of REE + Y analysis representative sites (white box): 62.30c; 22S.E; BG.4; BG.6. (*E*-F) Group 2 hand sample photographs of REE + Y analysis representative sites (white box): BG.1; BG.5. (G-H) Group 1 representative petrography: G - Hematized dolomite rhombs (arrow) throughout a microquartz matrix (BG.4). H - Hematized dolomite rhomb cut by chalcedony and microquartz veins (arrow) (BG.6). Scale bars, 500 μm. xpl. (I-J) Group 2 representative petrography: I - Hematized dolomite rhomb (arrow) and quartz vein (Qv) in a microquartz matrix (BG.5). Scale bar, 100 μm. xpl. J - Sub-rounded and unsorted intraclasts (arrows) set within a very fine-grained (1–100 μm) microquartz matrix (BG.1). Scale bar, 500 μm. ppl. (K) Hand sample of carbonate-chert couplets ('zebra rock') showing representative sites of REE + Y analysis (black boxes FoV, ~5 mm). 62S.1 CO3 – silicified carbonate (ankerite) layer. 62S.1 Ch – chert layer. The carbonate-chert couplet layers are linked, displaying gradational contacts between carbonate-chert and sharp contacts between chert-carbonate of the overlying couplet (Van Kranendonk, 2006). (L) Diagenetic crystal casts after aragonite (approx. 3 cm across) interbedded with partially silicified ankerite layers of the zebra rock.

from the lower two lithostratigraphic assemblages (A1-A2) i.e., bedded grey-black-white chert, carbonate-chert couplets, flat laminated grey chert, irregular layered grey chert, massive grey chert, and green-red cm-bedded chert; hot spring geyserite and sinter terracette deposits (Djokic et al., 2017: sites 16 N, 1S, and 23S of A2; Djokic et al., 2021); jaspilitic chert forming A3; and, silicified green volcaniclastic siltstone from A4. Detailed sample descriptions, location data, and stratigraphic context are detailed in Supp. Data 1.

4.1. Trace and rare earth element geochemistry

4.1.1. Assemblage 1–2 (A1-A2)

4.1.1.1. Bedded grey-black-white chert (A1-A2). Bedded grey-black-white chert samples ($n = 6$) fall into two groups with distinct REE + Y patterns (Fig. 6; Supp. Table 1). Group 1 samples (TD18-22S.E, 62.30c, BG.4, BG.6) display $(LREE)_{MUQ}$ depletion (Pr/Yb = avg. 0.17; Nd/Yb = avg. 0.26), positive La, Gd and Ce anomalies (La/La* = avg. 2.01; Gd/Gd* = avg. 1.04; Ce/Ce* = avg. 1.26), variable Y anomalies (Y/Ho = 29.2–31.3), and strong positive Eu anomalies (Eu/Eu* = avg. 3.35) (Fig. 6A). Group 1 display relatively flat $(REE)_{CHON}$ patterns (La/Lu = avg. 3.2), with slight $(LREE)_{CHON}$ enrichment and strong positive Eu anomalies (Eu/Eu* = avg. 2.49) (Fig. 6B). In contrast, group 2 samples (BG.1, BG.5) display convex-upward $(REE + Y)_{MUQ}$ patterns (Pr/Yb = avg. 1.15; Nd/Yb = avg. 1.39) with no Y anomaly (Y/Ho = 24.2–27), but with positive Eu, La, and Gd anomalies (Eu/Eu* = avg. 2.98; La/La* = avg. 1.83; Gd/Gd* = avg. 1.05) (Fig. 6C). Group 2 displays $(LREE)_{CHON}$ enrichments (La/Lu = avg. 9.39) with strong positive Eu anomalies (Eu/Eu* = avg. 2.18) (Fig. 6D). Sample BG.5 has a negative Ce_{MUQ} (Ce/Ce* = 0.55) and negative Ce_{CHON} anomaly.

4.1.1.2. Cm-bedded alternating carbonate-chert couplet unit, 'zebra rock' (A2). Carbonate (silicified) and chert samples ($n = 2$) from the 'zebra rock' unit display $(LREE)_{MUQ}$ depletion (Pr/Yb = avg. 0.22; Nd/Yb = avg. 0.24), positive La, Gd, and Eu anomalies (La/La* = avg. 1.69; Gd/Gd* = avg. 1.02; Eu/Eu* = avg. 2.07), negative Ce anomalies (Ce/Ce* =

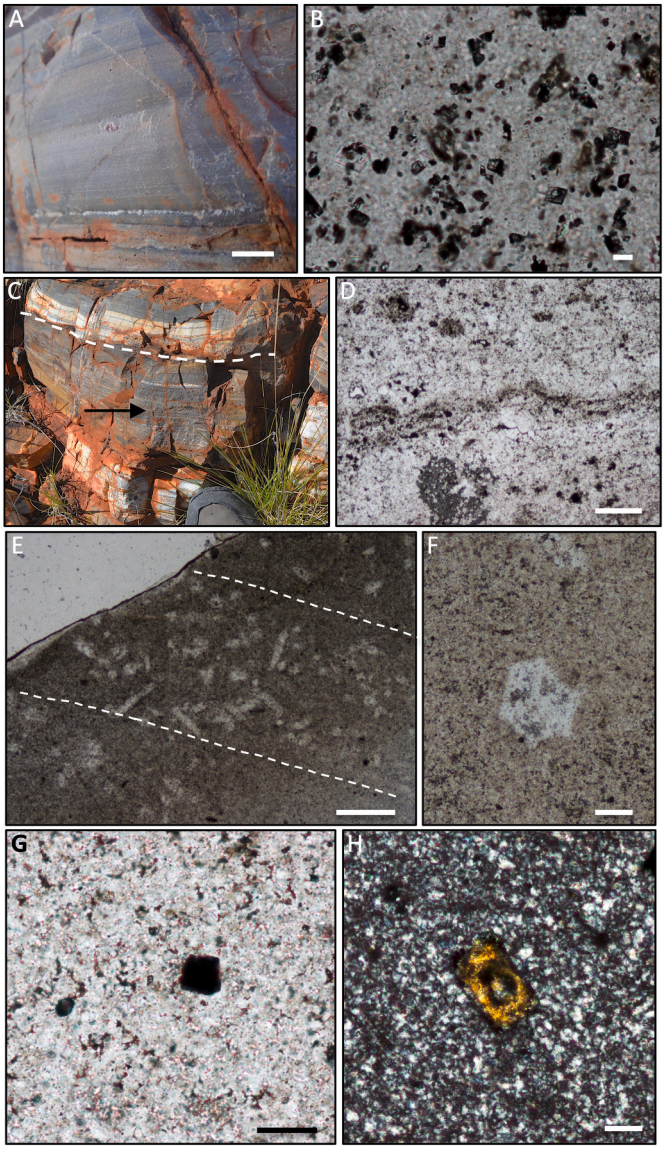


Fig. 4. DFc1 grey bedded cherts. (A-B) Flat laminated, grey-white bedded chert: A - Outcrop photograph. Scale bar, 3 cm. B - Micrograph displaying matrix-supported composition with fine-grained, indeterminate grains, shards, and rhombs. Scale bar, 20 μm. ppl. (C-D) Irregularly layered, grey-white bedded chert: C - Outcrop of this chert (arrow) interbedded with flat laminated grey chert (above the stippled line). Tip of shoe for scale. D - Micrograph showing faint irregular bedding and fine-grained ferruginous material set within microquartz matrix. Scale bar, 500 μm. ppl. (E-H) Massive grey chert. Micrographs: E - Fine layering with outlines of silicified lath-shaped crystals. Scale bar, 500 μm. ppl. F - Cross-section of laths showing hexagonal shape. Scale bar, 100 μm. ppl. G – Hematized pyrite. Scale bar, 50 μm. ppl. H - Altered ferromagnesian silicate mineral. Scale bar, 50 μm. xpl.

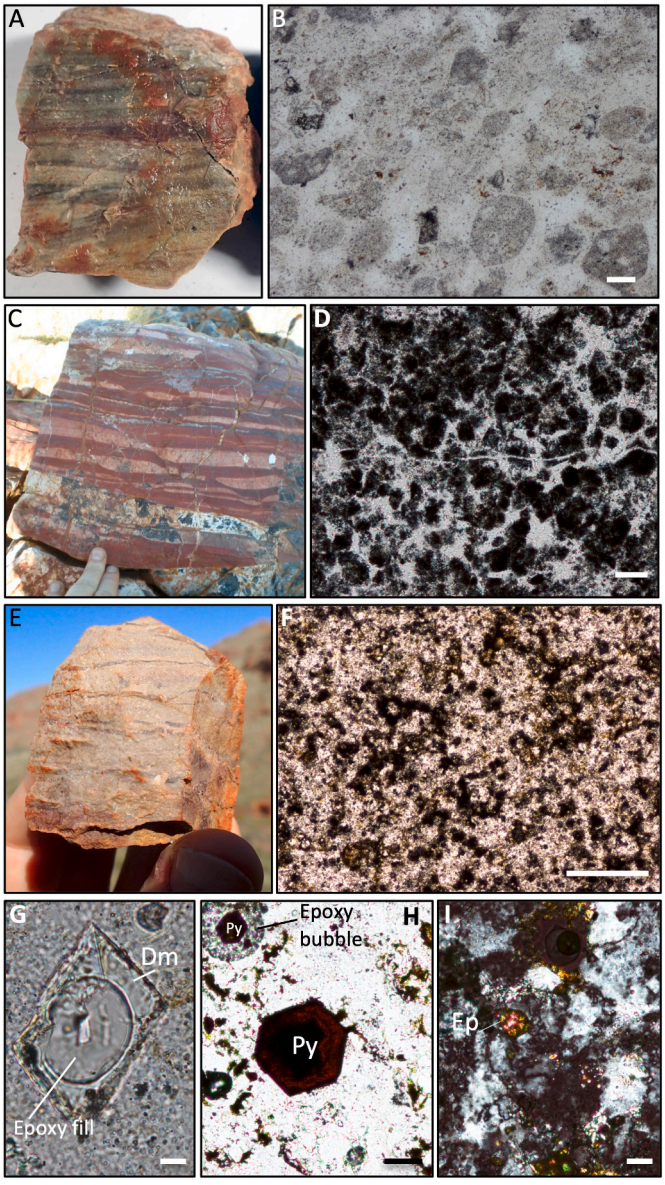


Fig. 5. DFc1 volcaniclastic chert and jaspilitic chert. (A-B) Green-red cm-bedded chert. A - Hand sample showing fine green and red layering. B - Micrograph displays rounded and subrounded volcanic grains, some with vesicular basaltic textures. Scale bar, 100 μm. ppl. (C-D) Jaspilitic chert (A3). C - Outcrop image showing mm to cm bedded opaque to translucent red bedding. D - Fe-oxide (hematite) rich, faintly rhombic grains within the layering of jaspilitic chert. Scale bar, 50 μm. ppl. (E-I) Green volcaniclastic siltstone (A4). E - Hand sample showing layering cut by mm-thick quartz veins. Micrographs: F - Fine-grained, clotted opaque minerals set within a microquartz matrix. Scale bar, 1 mm. ppl. G -Silicified dolomite rhomb (Dm). Scale bar, 10 μm. Ppl. H - Hematized euhedral pyrite (Py). Scale bar, 50 μm. Ppl. I - Epidote grains (Ep). Scale bar, 20 μm. xpl. (For interpretation of the references to colour in this figure legend, the reader is referred to the web version of this article.)

avg. 1.09), and minor positive Y anomalies (Y/Ho = 32.6–34) (Fig. 6E; Supp. Table 1). The silicified carbonate sample (62S.1 CO3) displays higher REE contents than the chert sample (62S.1 CH). $(REE + Y)_{CHON}$ display relatively flat (silicified ankerite: La/Lu = 1.23) to concave-downward (chert: La/Lu = 2.54) patterns with strong positive Eu anomalies (Eu/Eu* = avg. 1.54) (Fig. 6F).

4.1.1.3. Flat laminated grey chert (A2). Flat laminated grey chert samples (TD18-10 N.4, 29S.A4) have weak $(LREE)_{MUQ}$ depletion (Pr/Yb = avg. 0.54; Nd/Yb = avg. 0.55), weak positive La anomalies (La/La* = avg. 1.16), weak or absent Gd (Gd/Gd* = avg. 1.04) and positive Eu anomalies (Eu/Eu* = avg. 2.75), and chondritic to slightly superchondritic Y/Ho values (24.8–31.7) (Fig. 7A; Supp. Table 1). $(REE + Y)_{CHON}$ patterns display enriched $(LREE)_{CHON}$ (La/Lu = avg. 4.23), positive Eu anomalies (Eu/Eu* = avg. 2.00), and flat $(MREE)_{CHON}$ to $(HREE)_{CHON}$ (Fig. 7B).

Irregularly layered grey chert samples (TD18-10 N.3, TD18-21S.A.2, BG.7) display $(REE + Y)_{MUQ}$ patterns with $(LREE)_{MUQ}$ enrichment (Pr/Yb = avg. 2.52; Nd/Yb = avg. 2.93), positive La and Eu anomalies (La/La* = avg. 1.41; Eu/Eu* = avg. 2.33), weak positive, or absent Gd (Gd/

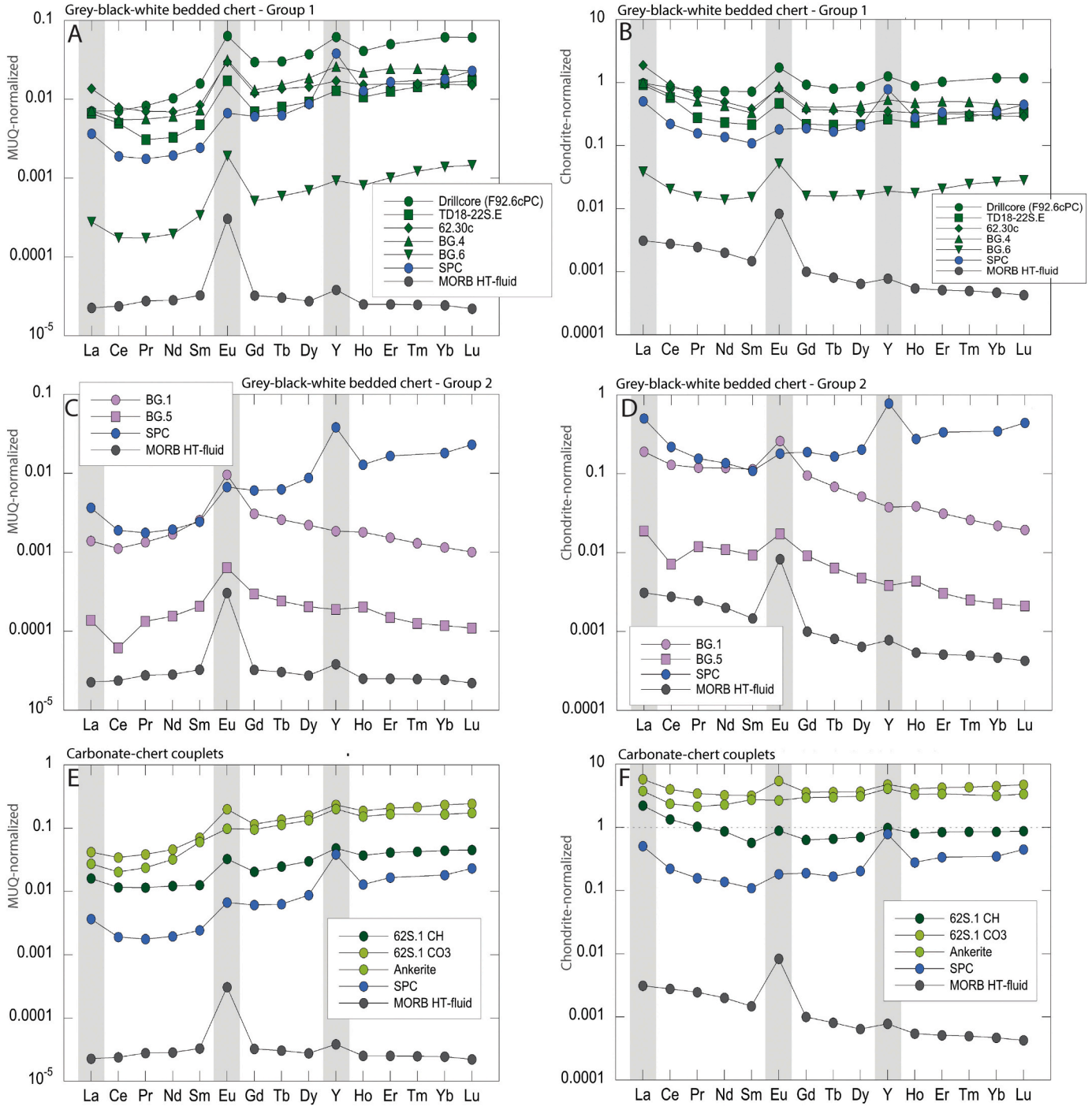


Fig. 6. REE and trace elements of DFc1 grey-black-white chert and carbonate-chert couplets. (A-D) REE + Y plots of bedded grey-black-white chert. (A-B) Group 1 samples and an unweathered drill core sample (Rividi, 2010: Appendix 3, sample F92.6cPC) from DFc1 are comparable to Archean seawater stromatolitic carbonates (SPC). (C-D) Group 2 bedded grey-black-white chert samples display hydrothermal patterns comparable to mid-ocean ridge hydrothermal fluids (MORB HT fluid). (E-F) REE + Y plots of the carbonate-chert couplets ('zebra rock'). Chert layer - 62S.1 CH. Silicified carbonate (62S.1 CO3) and primary carbonate (Ankerite) samples (Van Kranendonk et al., 2003) are comparable to Archean seawater carbonates (SPC) but contrast with mid-ocean ridge hydrothermal fluid patterns (MORB HT fluid). Note the more positive Eu anomaly in the silicified carbonate (62S.1 CO3) compared with the primary carbonate (ankerite), indicating silicification has not significantly affected the overall REE + Y content in 62S.1 CO3. Plot data references: SPC and Ankerite - Van Kranendonk et al., 2003: Table 1, sample 177882–1/4 and sample 177887, respectively; MORB HT fluid - Douville et al., 1999: Table 3, sample ND17G2, Mg-free end-member.

Gd* = avg. 1.17), and chondritic Y/Ho ratios (25.5–29.9) (Fig. 7C; Supp. Table 1). $(REE + Y)_{CHON}$ patterns exhibit strong LREE enrichment with steep positive profiles (La/Lu = avg. 32.69) and positive Eu anomalies (Eu/Eu* = 1.70) (Fig. 7D).

4.1.1.4. Massive grey chert (A2). Massive grey chert samples (BG.2, BG.8) display relatively flat $(REE + Y)_{MUQ}$ patterns with convex-upward, profiles defined by a positive $(LREE)_{MUQ}$ slope and a negative slope across the MREE to HREE (Pr/Yb = 1.26; Nd/Yb = avg. 1.48) (Fig. 7E; Supp. Table 1). They display positive Eu anomalies (Eu/Eu* = avg. 1.83), and no La, Ce, Gd or Y anomalies (La/La* = avg. 1.05; Ce/Ce* = avg. 1.05; Gd/Gd* = avg. 0.98; Y/Ho = avg. 21). $(REE + Y)_{CHON}$

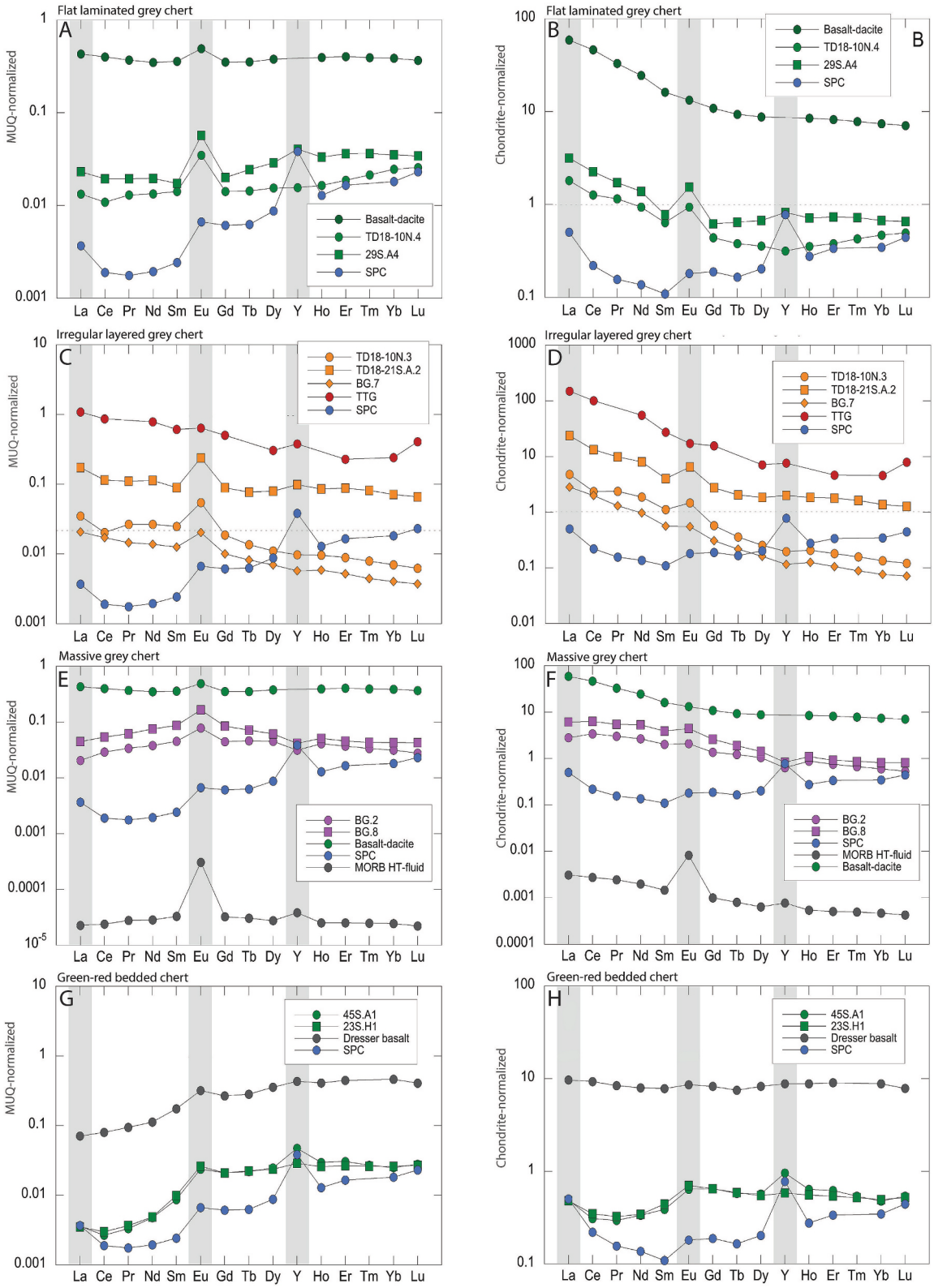


Fig. 7. REE and trace elements of DFc1 grey cherts and green-red bedded chert. (A-B) Flat laminated, grey-white bedded chert patterns contrast with Archean seawater carbonate (SPC) patterns but resemble patterns of evolved basalt-dacite suites. (C-D) Irregular layered, grey-white bedded chert samples also contrast with Archean seawater patterns (SPC) but are comparable to patterns of Archean Tonalite-Trondjemite-Granodiorite (TTG). (E-F) Massive grey cherts contrast with Archean seawater carbonate (SPC) signatures but have REE + Y that resemble mid-ocean ridge hydrothermal fluid patterns (MORB HT-fluid) and evolved basalt-dacite. (G-H) Green-red bedded chert is comparable to Archean seawater carbonate (SPC) signatures but resembles some features of relatively unaltered Dresser Formation basalt. Plot data references: SPC - Van Kranendonk et al., 2003: Table 1, sample 177882–1/4; Basalt-dacite - Hollings and Kerrich, 2000: Table 3, sample SB95-17; TTG - Martin et al., 2005: Table 1, samples TTG > 3.5 Ga; MORB HT-fluid - Douville et al., 1999: Table 3, sample ND17G2, Mg-free end-member; Dresser basalt - Van Kranendonk and Pirajno, 2004: Table 1, sample 159638.

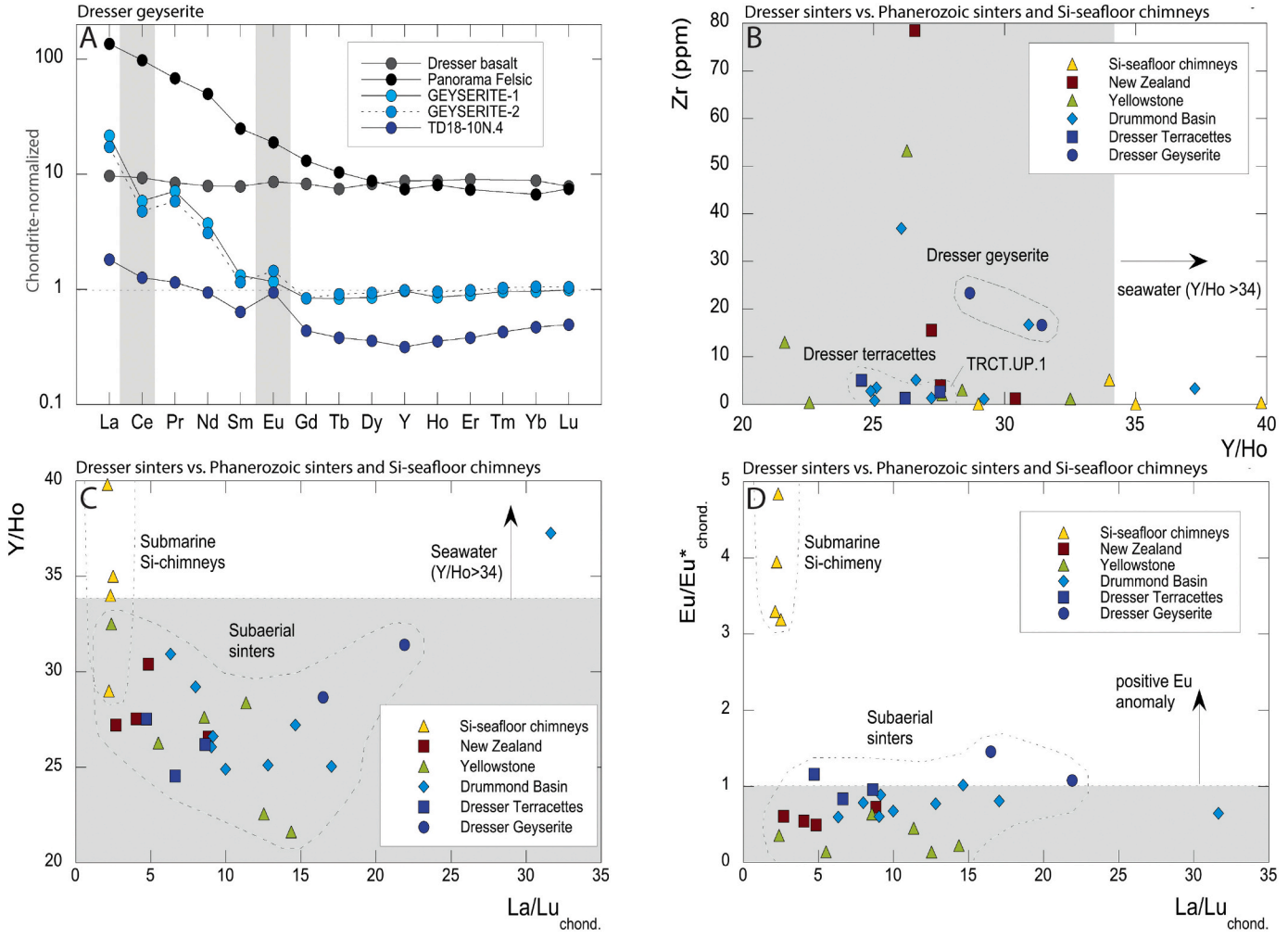


Fig. 8. Dresser hot spring sinters versus Phanerozoic sinters and Si-seafloor chimneys. (A) MUQ- and chondrite-normalized REE + Y of Dresser geyserite (GEYSERITE-1 and -2) versus a Dresser basalt (Van Kranendonk and Pirajno, 2004: Table 1, sample 159638), grey-white bedded chert (sample TD18-10N.4 - resembling evolved basalt-dacite suites), and a felsic unit from the Panorama Formation (Panorama Felsic) (Smithies et al., 2019: Table 20.3, sample 179895). X-Y plots show (B) Y/Ho versus Zr (C) $(La/Lu)_{CHON}$ versus Y/Ho and (D) $(La/Lu)_{CHON}$ versus $(Eu/Eu^*)_{CHON}$ for Dresser hot spring deposits (Dresser Geyserite and Terracettes), Phanerozoic subaerial hot spring sinter deposits including modern-Pleistocene Taupo and Coromandel volcanic zone sinters of New Zealand, modern-recent sinters from Yellowstone National Park, USA and Devonian sinters from the Drummond Basin, QLD, Australia (Djokic et al., 2021: Supp. Table S1), and Si-rich seafloor hydrothermal chimney vent deposits (Si-seafloor chimneys) from the East Pacific Rise, 18 S (Dekov et al., 2015: Table 1, samples ND16–08-1, ND16–08-3, ND16–08-4, ND16–08-5). For seawater value (Y/Ho > 34) and positive Eu anomaly see Bau (1996), Bolhar et al. (2004), Kamber et al. (2005), and Murray et al. (1991).

patterns display enriched $(LREE)_{CHON}$ over $(HREE)_{CHON}$ and small positive Eu anomalies (Eu/Eu* = avg. 1.33) (Fig. 7F).

4.1.1.5. Green-red bedded chert (A2). Green-red cm-bedded chert samples (45S.A1, 23S·H1) display $(REE + Y)_{MUQ}$ patterns with $(LREE)_{MUQ}$ depletion (Pr/Yb = avg. 0.14; Nd/Yb = 0.19) and positive La, Eu, and Ce anomalies (La/La* = avg. 5.57; Eu/Eu* = avg. 1.64; Ce/Ce* = avg. 1.32), weakly positive Gd anomalies (Gd/Gd* = avg. 1.05) and superchondritic Y/Ho (29.2–41.7) (Fig. 7G; Supp. Table 1). $(REE + Y)_{CHON}$ patterns display LREE depletion (La/Lu = 0.92) and positive Eu anomalies (Eu/Eu* = avg. 1.29) (Fig. 7H).

4.1.1.6. Dresser hot spring deposits (A2). Dresser geyserite samples (GEYSERITE-1, GEYSERITE-2) display $(REE + Y)_{CHON}$ patterns with LREE enrichment (La/Lu = 21.9, 16.5, respectively) (Fig. 8A; Supp. Table 1). Ce is depleted relative to the neighbouring Pr. A flattening out over MREE to HREE is observed. Both samples display slight positive Eu anomalies (Eu/Eu* = 1.11^, 1.47). However, an Eu error of up to 20% in GEYSERITE-1^ is possible (see Supp. Data 1 for details). $(REE + Y)_{MUQ}$ patterns are not used in this study, and are documented in Djokic et al. (2021). Zr values are 16.7 and 23.4.

Dresser sinter terracettes from the base to the top of a single hand sample (1S.TRCT-1, 1S.TRCT-2, 1S.TRCT.UP.1, respectively) display $(LREE)_{MUQ}$ depletion (Pr/Yb = 0.6, 0.91, 0.91; Nd/Yb = 0.64, 0.98, 0.98), a shift to slight positive La anomalies upsection (La/La* = 0.93, 1.08, 1.08), and chondritic Y anomalies (Y/Ho = 26, 25, 28) (Fig. 9A-B; Supp. Table 1). All samples show absent or weakly depleted Ce anomalies (Ce/Ce* = avg. 0.90) and small positive Eu anomalies (Eu/Eu* = 1.35, 1.17^, 1.59^{+}). However, Eu errors of up to 20% may exist in 1S.TRCT-2^ and 1S.TRCT.UP.1^{+} (see Supp. Data 1 for details). $(REE + Y)_{CHON}$ patterns are negatively sloping, with relatively flat HREE and no Eu anomalies. $(LREE)_{CHON}$ enrichment is less pronounced for sample 1S.TRCT.UP.1 (La/Lu = 4.70) relative to the underlying terracette samples (La/Lu = avg. 7.62). Zr values range 1.3–5.1.

4.1.2. Assemblage 3 (A3) facies

4.1.2.1. Jaspilitic chert. Jaspilitic chert samples (BG.3, 48S.2, TD18-

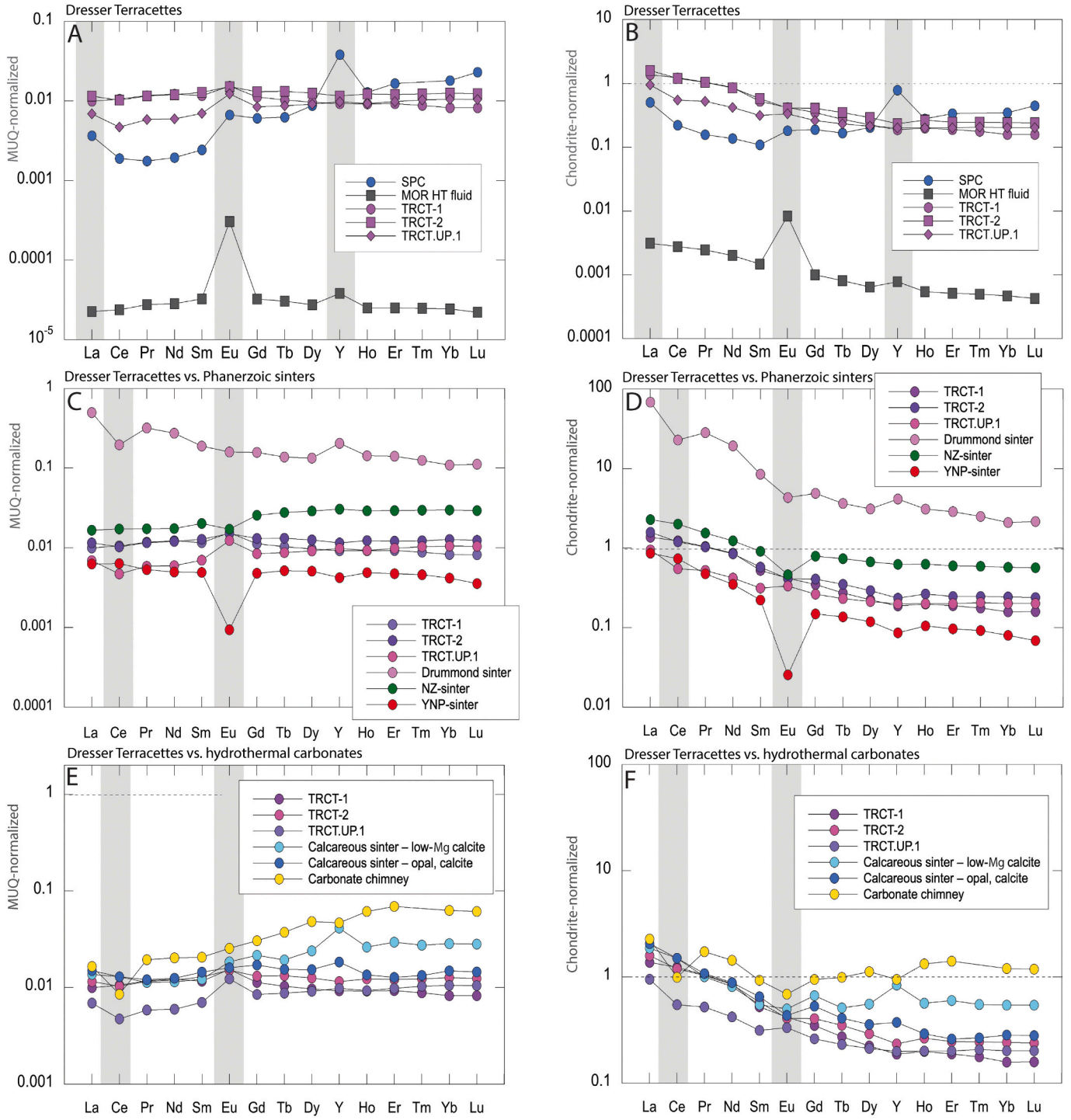


Fig. 9. REE and trace elements of Dresser terracettes versus Phanerozoic sinters and non-marine hydrothermal carbonate sinters. (A-B) REE + Y of Dresser terracettes show marked contrast with Archean seawater carbonate (SPC - Van Kranendonk et al., 2003: Table 1, 177882-1/4)) and $(LREE)_{CHON}$ enrichment, comparable to mid-ocean ridge hydrothermal fluids (MOR HT fluid) but lack the strong positive Eu and Y anomalies. (C-D) Dresser terracettes display flat $(REE)_{MUQ}$ patterns and $(LREE)_{CHON}$ enrichment broadly comparable to Phanerozoic sinter from the Devonian Drummond Basin of Queensland, Australia (sample 28.2/6/92), the Taupo Volcanic Zone in New Zealand (sample UMA-SINTER), and Yellowstone National Park in the USA (sample LGB-SC-4-18) (For plot data see Djokic et al., 2021: Supp. Table S1). (E-F) Comparison of the Dresser terracettes with non-marine hydrothermal carbonates. The lower terracette layers (TRCT-1, TRCT-2) resemble patterns of an opal, calcite hot spring sinter (Feng et al., 2014: Table 4, sample YBJ-6C). The upper layer (TRCT.UP.1) resembles a low-Mg calcite hot spring sinter (Feng et al., 2014: Table 4, sample CP-1) and a lacustrine hydrothermal carbonate chimney deposit from Lake Tanganyika (Barrat et al., 1999: Table 4, sample 'Avg. ext. wall carbonate').

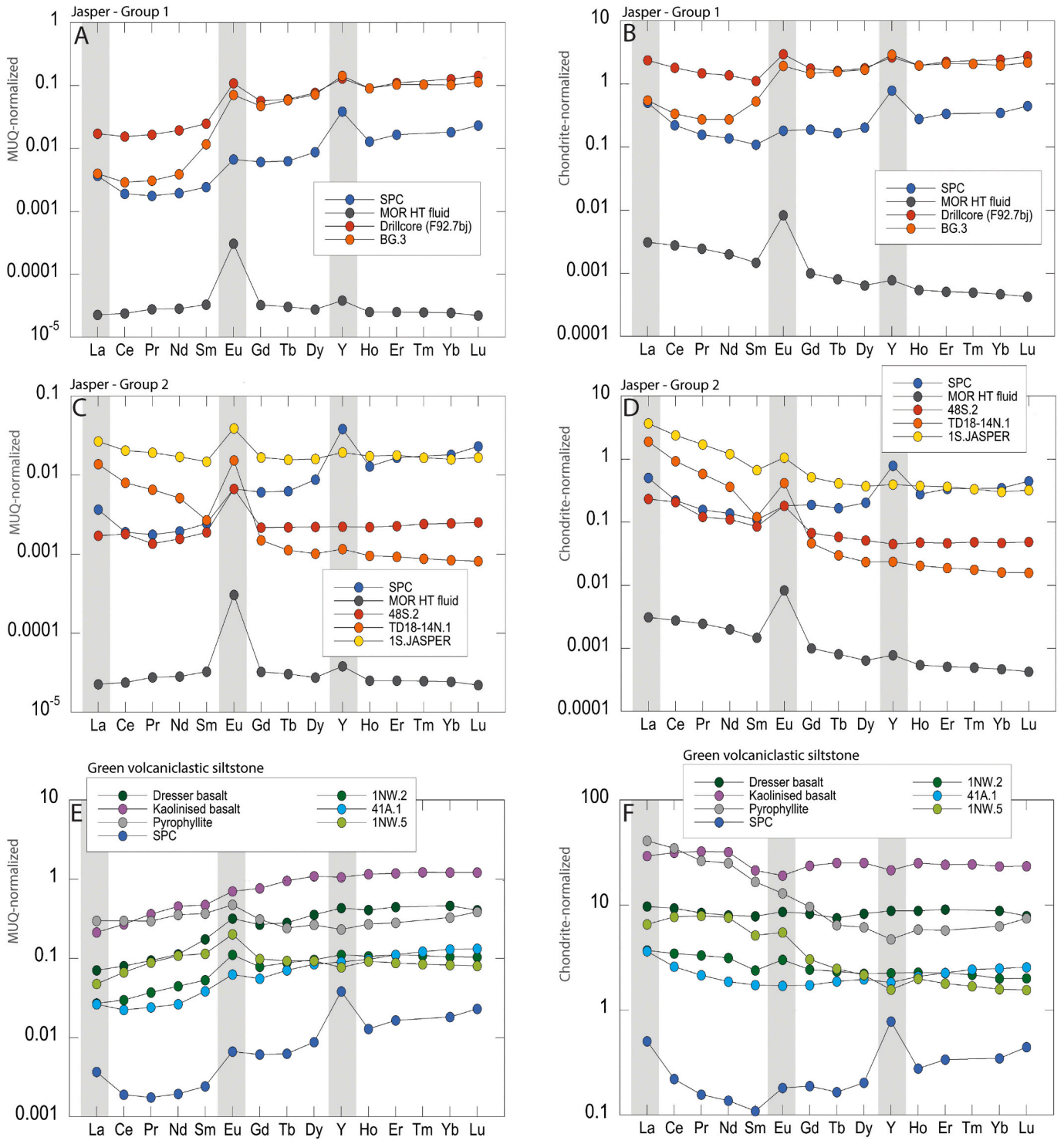


Fig. 10. REE and trace elements of DFc1 jaspilitic chert and volcaniclastic chert. (A-D) REE + Y plots of jaspilitic chert (A3) display two groups. (A-B) Group 1 displays mixed seawater-hydrothermal patterns. Seawater features include $(LREE)_{MUQ}$ with positive La and Y comparable to Archean seawater carbonates (SPC). Hydrothermal features include strong positive Eu. Group 1 is also comparable to an unweathered drill core sample of jaspilitic chert (Rividi, 2010: sample, F92.7bj) but which has less $(LREE)_{MUQ}$ fractionation, more flattened chondrite-normalized patterns, and a stronger positive Eu anomaly. (C-D) Group 2 patterns resemble mid-ocean ridge hydrothermal fluids (MOR HT fluid) but without strong positive Eu and Y anomalies. (E-F) REE + Y plots of Dresser green volcaniclastic siltstone (A4) are variable, with some seawater-like features (cf. SPC) i.e., $(LREE)_{MUQ}$ depletion, but also with features that resemble relatively unaltered Dresser basalt patterns that have smooth $(LREE)_{MUQ}$ depletion. Dresser volcaniclastic siltstone patterns may therefore be composed of altered basaltic material from the Dresser Formation e.g., cf. Dresser altered basalts (Kaolinised basalt) and pyrophyllite-quartz-sericite schistose basalts (Pyrophyllite) from elsewhere in the Pilbara. Plot data references: SPC - Van Kranendonk et al., 2003: Table 1, sample 177882–1/4; MOR HT fluid - Douville et al., 1999: Table 3, sample ND17G2, Mg-free end-member; Dresser basalt and Pyrophyllite- Van Kranendonk and Pirajno, 2004: Table 1, sample 159368 and sample 177893, respectively. (For interpretation of the references to colour in this figure legend, the reader is referred to the web version of this article.)

14N.1, 1S.JASPER) display two broad groups (Fig. 10A-D; Supp. Fig. 2; Supp. Table 1). Group 1 (sample BG.3) displays $(LREE)_{MUQ}$ depletion (Pr/Yb = 0.03; Nd/Yb = 0.04), positive La and Eu anomalies (La/La* = 2.78; Eu/Eu* = 2.41), weak to absent Gd and Ce anomalies (Gd/Gd* = 1.05; Ce/Ce* = 1.28), and superchondritic Y/Ho ratios (41.2). $(REE + Y)_{CHON}$ patterns show strong LREE depletion (La/Lu = 0.25) and a positive Eu anomaly (Eu/Eu* = 2.19).

Group 2 samples (48S.2, TD18-14N.1, 1S.JASPER) have relatively flat $(REE + Y)_{MUQ}$ patterns, but with minor LREE enrichment (Pr/Yb = avg. 3.19; Nd/Yb = avg. 2.61), weakly positive to absent La and Gd anomalies (La/La* = avg. 1.48; Gd/Gd* = avg. 1.10), chondritic to weakly superchondritic Y/Ho ratios (26.4–31.8), and positive Eu anomalies (Eu/Eu* = avg. 4.38). $(REE + Y)_{CHON}$ patterns display strong LREE enrichment (La/Lu = avg. 45.6) and positive Eu anomalies (Eu/Eu* = avg. 3.26).

4.1.3. Assemblage 4 (A4) facies

4.1.3.1. Green, silicified volcaniclastic siltstone. Green, silicified volcaniclastic siltstone samples (41A.1, 1NW.2, 1NW.5) display varied REE + Y patterns (Fig. 10E; Supp. Table 1). Samples 41A.1 and 1NW.2 display $(REE + Y)_{MUQ}$ patterns with LREE and MREE depletion relative to HREE (Pr/Yb = avg. 0.27; Nd/Yb = avg. 0.31), small positive La anomalies (La/La* = avg. 1.29) and chondritic Y/Ho ratios (~26). Sample 1NW.5 displays minor $(LREE)_{MUQ}$ enrichment (Pr/Yb = 1.07; Nd/Yb = 1.31), no La anomaly (La/La* = 0.97), and subchondritic Y/Ho ratios (~21.9). $(REE + Y)_{CHON}$ patterns display some variability (Fig. 10F). Sample 1NW.2 displays negative Sm and positive Eu anomalies relative to neighbouring elements. Sample 41A.1 displays a concave upward pattern from the HREEs to LREEs and small negative Y. Sample 1NW.5 is enriched in LREE with a concave up trend from Sm-La. Samples 1NW.2 and 41A.1 have generally flat $(REE + Y)_{CHON}$ patterns, whereas sample 1NW.5 displays $(LREE)_{CHON}$ enrichment (La/Lu = 4.21).

5. Discussion

5.1. Reliability of REE + Y data

Although the expected behaviour of REE + Y fractionation in modern depositional environments is relatively well understood, various pre- and post-depositional processes can alter the REE + Y composition of ancient rocks. Therefore, we consider factors influencing REE + Y fractionation, including differential partitioning, crustal contamination, and post-depositional alteration.

Differential REE + Y partitioning from solution into various mineral phases can affect the overall REE + Y content. Fe-oxides are known to readily sorb REE onto their surface, causing sub-chondritic Y/Ho ratios, even when seawater is enriched with Y (Prakash et al., 2012). REE + Y partitioning into Fe-oxides and chert (silica) during deposition is ruled out for all lithofacies studied here, except for Fe-oxides in jasper (see Section 5.2.2; Jaspilitic chert) (Johnson et al., 2022a; Johnson et al., 2022b). In most DFc1 lithofacies, Fe-oxides/hydroxides are secondary mineral phases that result from diagenetic alteration (Van Kranendonk et al., 2008) or surface oxidative processes e.g., Fe-oxides/hydroxide pseudomorphs after carbonate or pyrite (Fig. 5H). In this study, the impact of hematization on REE + Y patterns of altered metacarbonate rocks appears negligible. Despite containing hematized siderite, weathered samples compared with their unweathered (drillcore) equivalents show largely consistent REE + Y patterns (Fig. 6A-B).

"Cherts" represent a large proportion of DFc1 units and reflect post-depositional silicification of precursor sedimentary rocks during hydrothermal fluid flow (Buick and Barnes, 1984; Van Kranendonk et al., 2008). However, some silica may have precipitated directly out of hydrothermal solution during sedimentary deposition as amorphous silica and/or geyserite. There is limited experimental data for REE + Y partitioning into amorphous silica from solution, though the following reasons suggest that this does not affect the overall REE + Y. LREE/HREE ratios are relatively unaffected during binding of REE to silica at low pH and low dissolved Si (DSi) of 4 μmol/kg (Akagi, 2013). It is not known if the high DSi concentrations estimated in Archean oceans (>1500 μmol/kg) (Siever, 1992; Maliva et al., 2005) would affect REE fractionation. However, REE + Y patterns of Archean and modern carbonates appear unaffected by temporal variations in the ocean Si inventory (e.g., Bolhar et al., 2004). Likewise, REE + Y patterns of terrestrial siliceous sinters closely mimic those of the basement (igneous) rocks and geothermal fluids, regardless of Si content in solution (Fig. 2C-D) (Lewis et al., 1997; Lewis et al., 1998).

As is the case for many deposits of similar age to the Dresser Formation, siliciclastic input may be obscured by diagenesis and silicification. Studies can use correlations (or anti-correlations) of immobile elements such as Th, Zr, Hf, and Sc representative of upper continental crustal components (Bolhar et al., 2004), or Ti/Zr ratios that fall in the range for igneous rocks to signal crustal 'contamination' (Smithies et al., 2007; Frimmel, 2009). Conversely, hot plate digestion and certain acid mixtures (2:1 HF-HNO3 sans HCl) can avoid leeching some refractory minerals (e.g., zircon, chromite, rutile) during analysis that concentrate these immobile elements. In this work, we opted for the latter to assess the chemical sedimentary lithofacies in our sample suite.

Post-depositional processes such as high-T and/or reducing hydrothermal fluids can cause remobilization of Eu (Bilal, 1991; MacRae et al., 1992), imprint marine REE + Y on igneous rocks (Brengman and Fedo, 2018 and references therein), and alter LREE contents (e.g., Van Kranendonk and Pirajno, 2004). However, we rule out any significant post-depositional effects in our study because REE + Y signatures from samples of the same lithofacies that are separated by hundreds to thousands of meters exhibit a high degree of reproducibility (Figs. 6, 7, and 10; Supp. Data 1) (See also stratigraphy published in Djokic et al., 2021: Supp. Figs. 1 and 2). In addition, samples with petrographic evidence for clastic input yield igneous REE + Y patterns (discussed in Section 5.2).

5.2. Origin of REE + Y in Dresser lithofacies

Previous lithostratigraphic and geochemical evidence for distinct contributions from marine, subaerial, hydrothermal, and clastic depositional environments is supported by the REE + Y profiles of the 10 Dresser lithofacies analyzed here, as discussed below.

5.2.1. Assemblage 1–2

5.2.1.1. Marine carbonate deposition in hydrothermal basin/s (Bedded grey-black-white chert, A1-A2). Grey-black-white bedded chert display REE + Y patterns comparable to either mixed seawater-hydrothermal fluids (Group 1; $n = 4$) or high-temperature (>300 °C) mid-ocean ridge hydrothermal fluids (Group 2; $n = 2$) (Figs. 3A-J and 6A-D; Supp. Table 1; Supp. Data 1). Group 1 samples contain abundant hematized rhombic carbonate (siderite or ankerite), and their $(REE + Y)_{MUQ}$ patterns resemble silicified marine stromatolitic carbonates from the c. 3.43 Ga Strelley Pool Formation, situated geographically nearby DFc1 (Figs. 3G-H and 6A-B; Supp. Table 1). In contrast to the Strelley Pool carbonates, Group 1 samples display subdued La and Y anomalies, and more positive Eu anomalies. These features in addition to increased overall REE contents may be attributed to crustal contamination (cf. Van Kranendonk et al., 2003; Allwood et al., 2010). These strong positive $(Eu/Eu^*)_{MUQ}$ anomalies (2.92–4.45) indicate either primary input from high-temperature hydrothermal fluids (Fig. 6A-B) or later hydrothermal silicification (Bau and Dulski, 1996). Evidence for hydrothermal quartz veins cross-cutting rhombic carbonate supports the latter interpretation (Fig. 3H). However, secondary silicification does not typically produce such strong Eu anomalies - for example, the silicified carbonate-chert

couplets in this study have $(Eu/Eu^*)_{MUQ} = 1.98–2.15$. The slight positive Ce anomaly in sample TD18-22S.E is attributed to post-depositional oxidative weathering (e.g., Planavsky et al., 2020) given that unweathered bedded grey-black-white chert from drill core lacks this feature (Fig. 6A-B) (Rividi, 2010).

Group 2 samples display slight $(LREE)_{CHON}$ enrichment and minor positive Eu, resembling high-temperature (>300 °C) mid-ocean ridge hydrothermal fluids (Fig. 6C-D; Supp. Table 1; Supp. Data 1) (Douville et al., 1999). In contrast, $(REE + Y)_{MUQ}$ of group 2 samples lack positive Y and show slight concave upward patterns with positive La and Eu (Fig. 6C) that may reflect either primary hydrothermal exhalative deposits and/or post-depositional hydrothermal alteration. Evidence for cross-cutting quartz veins at least in part supports the latter interpretation (e.g., Fig. 3I). However, we suggest that $(REE + Y)_{CHON}$ of group 2 samples reflect a strong hydrothermal influence based on their MOR hydrothermal fluid pattern and positive $(Eu/Eu^*)_{MUQ}$ anomalies. The negative Ce anomaly in sample BG.5 is attributed to post-depositional oxidative weathering (e.g., Planavsky et al., 2020).

In summary, grey-black-white bedded cherts likely reflect the mixing of seawater with hydrothermal fluid exhalation (e.g., Van Kranendonk et al., 2003; Bolhar et al., 2005; Allwood et al., 2010) during the development of near-shore basins adjacent to shallow water and subaerial deposition (Supp. Data 1).

5.2.1.2. Semi-restricted, evaporative marine-hydrothermal basins (Carbonate-chert couplets, A2). Carbonate (silicified ankerite)-chert couplet samples ($n = 2$; Fig. 3K-L; Supp. Data 1) display REE + Y patterns similar to Archean stromatolitic seawater carbonates, with slightly depleted $(LREE)_{MUQ}$ and positive La, Y, and Eu anomalies (Fig. 6E-F; Supp. Table 1) (Van Kranendonk et al., 2003; Van Kranendonk et al., 2019). The increased LREE concentration (Fig. 6E-F) suggest minor crustal input (Van Kranendonk et al., 2003). The strong positive $(Eu/Eu^*)_{MUQ}$ anomaly of 2.07 in the silicified ankerite analyzed here (Fig. 6E-F, sample 62S.1 CO3; Supp. Table 1) is attributed to Eu remobilization during post-depositional silicification (Bau and Dulski, 1996). However, the slightly positive $(Eu/Eu^*)_{MUQ}$ anomaly of 1.26 recorded in a primary ankerite sample from previous work is attributed to synsedimentary hydrothermal activity (Van Kranendonk et al., 2003). In combination with the lithostratigraphic context (i.e., the presence of aragonite crystal casts, and association with shallow water to subaerial deposits; Supp. Data 1), the REE + Y data supports deposition in one or more shallow water, semi-restricted, evaporitic basins (volcanic caldera lakes), where seawater and hydrothermal fluids intermixed and evaporated to make a more highly concentrated brine (Van Kranendonk et al., 2003; Otálora et al., 2018; Van Kranendonk et al., 2019; Djokic et al., 2021).

5.2.1.3. Quiet water marginal-marine(?) facies (Flat laminated grey chert, A2). Flat laminated grey chert samples (n = 2) have $(REE + Y)_{MUQ}$ patterns that resemble those formed from a mix of Archean seawater carbonates and Late Archean evolved basalt-dacite suites e.g., weak $(LREE)_{MUQ}$ depletion with weak positive La and Y anomalies, positive Eu anomalies (Fig. 7A) (Hollings and Kerrich, 2000), and enriched $(LREE)_{CHON}$, flattened $(MREE)_{CHON}$ to $(HREE)_{CHON}$ and positive Eu anomalies (Fig. 7B; Supp. Table 1). The strong positive Eu likely reflects either primary in-mixing with hydrothermal fluids or post-depositional alteration. In combination with the stratigraphic context (association with other inferred shallow water facies bearing felsic volcaniclastic input such as massive grey chert; Supp. Data 1), the REE + Y data of flat laminated grey chert may reflect deposition in quiet water possibly marginal-marine conditions affected by evolved basaltic-dacitic ash or detritus in the earlier stages (A1-A2) of the Dresser caldera system. Indeterminate grains, volcanic ash shards, and siliceous and ferruginized dolomite (Fig. 4A-B) support input from carbonate and volcaniclastic sediment.

5.2.1.4. Shallow-water, intermediate-felsic volcaniclastic facies (Irregular layered grey chert, A2). Irregular layered grey bedded chert samples ($n = 3$) display REE + Y patterns that resemble Archean Tonalite-Trondjemite-Granodiorite (TTG) e.g., $(LREE)_{MUQ}$ enrichment and strong $(LREE)_{CHON}$ enrichment with steep profiles (Fig. 7C-D; Supp. Table 1; Supp. Data 1) (Martin et al., 2005). However, these samples display strong positive Eu anomalies indicating either remobilization of Eu during silicification (Bau and Dulski, 1996) or hydrothermal input.

Buick (1985) suggested a basaltic origin for the volcaniclastic component in similar bedded grey-white cherts (lutite), based on the presence of minor Fe-Ti-Mg mineralogy (sericite-chlorite-anatase-goethite). However, our data indicate more evolved igneous compositions for the silt-sized grains (Fig. 7C-D). Perhaps a variety of igneous components entered the sedimentary regime via terrestrial weathering and/or volcanic infall. We suggest that the REE + Y composition and the presence of ash reflect input from intermediate to felsic volcaniclastic material. The very fine grain size, thin bedding, poor sorting, and minor ripples support deposition in a low-energy, shallow-water environment (see also Buick, 1985).

5.2.1.5. Evaporite-bearing volcaniclastic facies (Massive grey chert, A1-A2). Massive grey chert samples (n = 2) display mixed REE + Y patterns, resembling evolved basalt-dacite compositions with $(LREE)_{CHON}$ enrichment and mid-ocean ridge hydrothermal fluid-type patterns including a positive Eu anomaly and $(LREE)_{CHON}$ enrichment (Fig. 7E-F; Supp. Table 1; Supp. Data 1) (Douville et al., 1999). These samples lack La, Ce, Gd, or Y anomalies characteristic of Archean seawater precipitates and display distinct $(REE + Y)_{MUQ}$ patterns indicative of a mixed sedimentary composition e.g., positive $(LREE)_{MUQ}$ slope and a negative slope across the MREE to HREE (Fig. 7E-F). Sediment variability is supported by a silicified muddy matrix, ferromagnesian silicates, and (pseudo-)hexagonal evaporative crystals (now silicified) (Fig. 4E-H). Given that the samples are laterally and temporally separated but share similar patterns (Fig. 7E-F), the silicified diagenetic crystal laths (Fig. 3E-F) and accessory minerals (constituting <10% in total) (Fig. 3G-H) do not likely affect the overall REE + Y patterns.

Massive grey chert has previously been described as gypsum-bearing siltstone with a fine-grained basaltic mud matrix similar to other grey bedded cherts (Buick, 1985: 'gypsiferous lutite'). However, the evolved basalt-dacite REE + Y profiles of massive grey chert are distinct from other grey bedded chert units (Fig. 7A-D) and Dresser basalts (see Fig. 7G-H). Rather, massive grey chert likely reflects quiet, shallow water deposition of evolved-basaltic mud with periods of evaporite deposition. Evaporative crystal-bearing layers (1–5 mm) interbedded with crystal-free layers (Fig. 4E) suggest local fluctuations in water chemistry driven by evaporation and thus shallow water conditions. This unit is interlayered with other low-energy, shallow water, or marginal marine facies (bedded grey cherts, stromatolites; Supp. Data 1).

5.2.1.6. Channelized mafic-volcaniclastic facies influenced by seawater (Green-red cm-bedded chert, A2). Green-red cm-bedded chert samples (n = 2) resemble a mix of Dresser basalt and seawater carbonate REE + Y patterns e.g., $(LREE)_{MUQ}$ depletion with variable La, Y, and Eu (Fig. 7G-H; Supp. Table 1; Supp. Data 1). These findings support previous work that described this unit as a basaltic wacke containing a silty volcanic ash matrix that has been silicified by circulating marine fluids (Buick, 1985). Seawater REE + Y features may be due to: 1. post-depositional alteration of the parent basaltic sediment via hydrothermal circulation (e.g., Brengman and Fedo, 2018) prior to reworking and transport into the sedimentary environment, or 2. Deposition within a mixed siliciclastic-carbonate (i.e., calc-silicate) environment (Olivier and Boyet, 2006). However, there is a lack of textural evidence for carbonate.

Cross and flat laminated beds indicative of meandering or braided rivers have been observed in this unit but were discounted as being of fluvial origin based on the absence of other recognized channelized

deposits (Buick, 1985). Recent work, however, has demonstrated the presence of channelized edgewise and pebble conglomerates interbedded with green-red cm-bedded chert (Djokic et al., 2021). Collectively, these observations may indicate that green-red cm-bedded chert represents a fluvial deposit influenced by seawater pre- or during deposition, though this is not conclusive.

5.2.1.7. Subaerial hot spring sinter facies (Dresser geyserite and sinter terracettes, A2). Dresser Geyserite: Previous work demonstrated that the context, texture, and geochemistry (including REE + Y) of Dresser geyserite closely resemble Phanerozoic-Modern hot spring deposits (Djokic et al., 2017; Djokic et al., 2021: Fig. 8) that precipitate from relatively low temperature terrestrial geothermal fluids (<250 °C at depth and ~ 120 °C at the surface) derived from meteoric ± magmatic water-bedrock interaction (e.g., Harris et al., 2009; Campbell et al., 2015). Data presented here for Dresser geyserite (n = 2) supports this interpretation and indicates the composition of the bedrock.

A terrestrial origin of Dresser geyserite is supported by non-marine Y/Ho values (<34) and relatively high Zr values (16–23) (Fig. 8B) (Djokic et al., 2021: Supp. Fig. 1). Felsic igneous rocks common in terrestrial settings are enriched in Zr relative to mafic igneous rocks, which is reflected in associated sedimentary rocks (Mielke, 1979). In contrast, high Y/Ho and low Zr in deep-sea hydrothermal Si-chimneys reflect marine, mafic-rock-hosted depositional settings (Fig. 8B) (Dekov et al., 2015). A correlation between terrestrial hot spring deposits and Dresser geyserite is further supported by their shared non-marine Y/Ho (< 34) and $(La/Lu)_{CHON}$ (Fig. 8C). Terrestrial sinters exhibit chondritic to sub-chondritic Y/Ho ratios (~24–34) reflecting the igneous host rock (Fig. 2) (McDonough and Sun, 1995). This is in contrast to deep-sea Si-chimneys that display high Y/Ho and relatively low La/Lu values consistent with marine origins (Dekov et al., 2015).

Precipitation of Dresser geyserite from low-temperature fluids is supported by low $(Eu/Eu^*)_{CHON}$ values and relatively enriched $(LREE)_{CHON}$ consistent with Phanerozoic sinters that form from low-temperature hydrothermal fluids (<250 °C) (Fig. 8D). In contrast, deep-sea Si-chimney deposits display strong positive Eu and low La/Lu values that form within high-temperature (>300 °C), marine conditions (Dekov et al., 2015). Possibly, the relatively lower temperatures (<250 °C) or lower water-to-rock ratio of terrestrial hydrothermal settings may result in less feldspar breakdown and Eu mobilization; temperature and pH rather than bedrock composition may influence this REE behaviour (Michard, 1989).

Given the origin of Dresser geyserite as a terrestrial geothermal sinter, its REE + Y patterns should reflect its igneous host rocks (Fig. 2) (Hopf, 1993; Christiansen, 2001). For example, New Zealand and Yellowstone National Park sinters display negative Eu anomalies consistent with their rhyolitic host rocks, whereas Drummond Basin sinters have no Eu anomalies and variable Ce and Y that reflect predicted intermediate-felsic volcanic bedrock (Fig. 2) (Ewers et al., 1992; e.g., Christiansen, 2001; Wilson and Rowland, 2016; Djokic et al., 2021).

Compared to relatively unaltered basalts from the Dresser Formation (Van Kranendonk and Pirajno, 2004: Table 1, sample 159638) the Dresser geyserite has highly fractionated $(LREE)_{CHON}$ (La/Lu = avg. 19.2) (Fig. 8). These patterns reflect more evolved felsic compositions e.g., Archean Panorama Formation rhyolite (Smithies et al., 2019: Table 20.3, sample 179895). Indeed, the local presence of evolved igneous components in DFc1 is supported by felsic volcaniclastic units throughout A1 and A2 (e.g., Fig. 7A-F) (Van Kranendonk et al., 2008) and high μ values ($^{238}U/^{204}Pb$) of 9.45 from Pb in barite (Thorpe, 1992). However, Dresser geyserite has more strongly fractionated LREE than any known felsic source from the Archean Warrawoona Group of the Pilbara Craton (Fig. 8) (Smithies et al., 2019). A possible explanation is the extreme advanced argillic alteration of DFc1 footwall basalts, which could have driven preferential breakdown of feldspars and thus enrichment of LREE into circulating geothermal fluids (Van Kranendonk and Pirajno, 2004; Caruso et al., 2021; Caruso et al., 2023).

Dresser Terracettes: REE + Y patterns of Dresser terracettes lack marine (positive Y and La, depleted $LREE_{MUQ}$) or high temperature (>300 °C) hydrothermal fluid patterns (positive Eu) (Fig. 9; Supp. Table 1). Indeed, these patterns are remarkably flat $(REE)_{MUQ}$ and only show slight $(LREE)_{CHON}$ enrichments, suggesting a source rock composition that is basaltic to slightly intermediate composition. However, a subdued seawater pattern appears in the uppermost layer based on minor LREE depletion and weak positive La.

The terracette REE + Y patterns in combination with Y/Ho versus Zr, $(La/Lu)_{CHON}$ versus Y/Ho, and $(La/Lu)_{CHON}$ versus $(Eu/Eu^*)_{CHON}$ ratios are consistent with a low-temperature, non-marine origin (Fig. 8B-D). The Dresser terracettes broadly compare to Phanerozoic sinters i.e., generally flat $(REE)_{MUQ}$ and enriched $(LREE)_{CHON}$ patterns, minor variable Ce and Eu anomalies, and chondritic Y (Fig. 9C-D; Supp. Table 1). However, they more closely resemble opal-calcite hot spring sinter deposits i.e., flat $(REE)_{MUQ}$ and $(LREE)_{CHON}$ enriched REE + Y patterns (Fig. 9E-F) (Feng et al., 2014). REE + Y patterns of the lower terracette layers (TRCT-1 and TRCT-2) most closely resemble that of an opal-calcite hot spring sinter (Feng et al., 2014: Table 4, sample YBJ-6C), whereas the upper terracette layer (TRCT.UP.1) resembles a low-Mg calcite hot spring sinter from the Tibetan Plateau, China (Feng et al., 2014) and hydrothermal lake carbonate chimneys from Lake Tanganyika of East Africa (Fig. 9E-F) (Barrat et al., 1999).

Minor differences between the upper terracette layer and hydrothermal carbonates include variable Ce, Gd and Y. REE + Y variability among hydrothermal carbonates is common (Barrat et al., 1999; Dekov et al., 2014; Feng et al., 2014). In the case of subaerial carbonate sinters, this variability can be attributed to complexation driven by factors such as salinity (e.g., Feng et al., 2014). The only other difference is the variable Eu (Fig. 9G-H). The small positive Eu in the upper terracette layer might be attributed to water-rock interaction causing preferential dissolution of feldspar, which can occur for subaerial sinters (Feng et al., 2014). However, an analytical artifact cannot be excluded (see section on Eu errors in Supp. Data 1).

These findings suggest that the Dresser Terracettes could have formed as either siliceous sinter or a non-marine, thermogene carbonate (travertine). A comparison with modern hot spring travertine is not possible due to a lack of REE + Y data on these types of deposits as pointed out by Teboul et al. (2016). The association of siliceous geyserite and terracettes may be explained by a fluctuating hot spring environment. Mixed silica-carbonate hot spring deposits can form on the macroscale and microscale driven by either fluctuating lake levels or precipitation e.g., Lake Bogoria, Kenya (Renaut and Jones, 1997) and the intertidal vent springs of Bahía Concepción Bay, Mexico (Canet et al., 2005), or the microchemical conditions e.g., Pavlova spring, Ngatamariki, New Zealand (Campbell et al., 2002).

REE + Y in hot spring sinter deposits vary widely across terrains and between pools due to bedrock composition, temperature, pH and Eh, sulfate concentration, and the levels of chloride, fluoride, and calcium in low salinity waters (White et al., 1964; Walter, 1976; Michard, 1989; Lewis et al., 1997; Lewis et al., 1998; Fouke et al., 2000; Guidry and Chafetz, 2003; Uysal et al., 2011), as well as microbial activity (Feng et al., 2014). This leads to distinct REE + Y compositions among different hydrothermal deposit types and between different geographical areas that otherwise contain similar hydrothermal settings e.g., Yellowstone National Park, USA versus New Zealand (Djokic et al., 2021: Supp. Fig. 7). This same variability has been observed for DFc1 hot spring deposits.

5.2.2. Assemblage 3: Deep water iron-carbonate facies (jaspilitic chert)

Jaspilitic chert displays two groups of REE + Y patterns (Fig. 10A-D). Group 1 (sample BG.3) displays mixed seawater-hydrothermal patterns e.g., $(LREE)_{MUQ}$ with positive La, Y, and Eu anomalies. This matches the pattern of unweathered jaspilitic chert from drill core (Rividi, 2010: sample, F92.7bj), although $(LREE)_{MUQ}$ is relatively more depleted in our

group 1 sample (Fig. 10A; Supp. Data 2; Supp. Table 1). Group 1 REE + Y data aligns with previous work that indicated a high-salinity end-member of jasper that reflects a marine source (Van Kranendonk et al., 2003; Bolhar et al., 2005; Djokic, 2015; Johnson et al., 2022a; Johnson et al., 2022b). The sub-micron crystals preserved within A3 jasper represent near-primary hematite (Fe-isotope and trace element data), although a detailed study of the iron isotopic composition of this unit indicated the primary iron-bearing phase was originally siderite, with the hematite having formed during early diagenesis (Johnson et al., 2022a; Johnson et al., 2022b).

Group 2 sample 1S.JASPER more closely resembles mid-ocean ridge hydrothermal fluids (Fig. 10C-D), whereas sample TD18.14N.1 aligns with previous work that indicated a contribution from a low-temperature hydrothermal fluid source interacting with more evolved volcanic rocks (Johnson et al., 2022a). The results from sample 1S. JASPER contrasts with previous work, which indicated a seawater profile (Johnson et al., 2022a). In this and previous work, sample 1S. JASPER was collected from a ~ 0.5 m-thick, laterally restricted unit (several meters) of jasper directly overlying subaerial hot spring geyserite and terracettes at site 1S (Fig. 11) (Djokic et al., 2017; Djokic et al., 2021). The contrasting REE + Y results may represent differences in the subsampling of the 1S.JASPER unit and could reflect a hydrothermal end-member or a variation in fluid sources during deposition.

A3 jaspilitic chert ranges 50 cm to several meters thick and is variably interbedded with marine carbonate facies (grey-white-black bedded chert; Section 5.2.1), shallow water, evaporite-bearing volcaniclastic facies (massive grey chert; Section 5.2.1), and channelized volcaniclastic facies (green-red bedded chert, A2) (Supp Data 1). Across DFc1, A3 jaspilitic chert is overlain by green volcaniclastic sandstone of A4. Deposition of A3 jaspilitic chert is thought to have occurred during times of subsidence, developing quiescent marine-hydrothermal basins during the later stages of the Dresser caldera system.

5.2.3. *Assemblage 4: Deep water mafic-volcaniclasitc facies (green volcaniclastic silstone)*

Green volcaniclastic siltstone samples 1NW.2 and 41A.1 have REE + Y patterns that resemble unaltered and more strongly (advanced argillic-)altered Dresser basalt (Fig. 10E-F; Supp. Table 1; Supp. Data 1) (Van Kranendonk and Pirajno, 2004). Hydrothermal alteration of a basaltic igneous source is supported by epidote grains (Fig. 5E-I; Supp. Data 1). Sample 1NW.5 resembles pyropyhillite-quartz-sericite altered basalt from the slightly younger (c. 3.4 Ga) Strelley Pool Formation (Van Kranendonk and Pirajno, 2004). The positive Eu anomaly in these samples may reflect components of the depositional environment and/or later silicification (e.g., Brengman and Fedo, 2018). The green volcaniclastic siltstone of A4 lies atop thick (10s–100s of meters) sections of green volcaniclastic pebble-cobble conglomerate and sandstone. Collectively, these units reflect the effects of rapid caldera collapse and infill by basaltic volcaniclastics (Supp Data 1) (Van Kranendonk, 2006; Van Kranendonk et al., 2019).

5.3. *Temporal REE + Y variations in DFc1 stratigraphy*

Three stratigraphic profiles enhanced by REE + Y data across the lateral extent of DFc1 illustrate a shallowing-upward transition (regressive sequence tract) from a submarine (i.e., footwall pillow basalt and A1 marine bedded cherts), to subaerial exposure (A2), followed by a deepening-upwards transition (transgressive sequence tract) back to submarine conditions (A3-A4) (Figs. 11 and 12).

The 'geyserite discovery' locality (16 N) preserves the transition

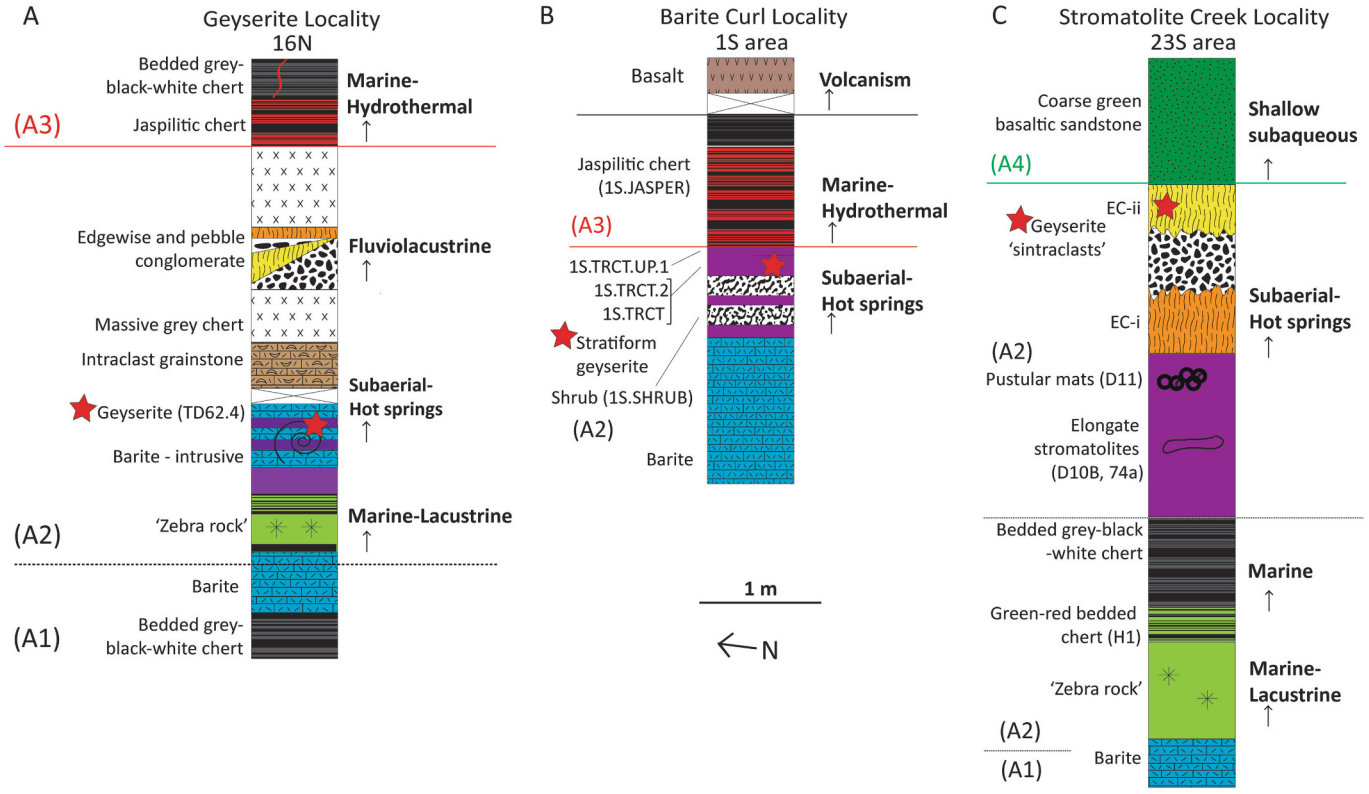


Fig. 11. Lithostratigraphy showing marine-terrestrial-marine transition up section within DFc1. (A) Section 16 N (The geyserite discovery locality) shows the transition from marine conditions (e.g., A1 bedded grey-black-white bedded chert) through to fluviolacustrine and subaerial hot spring development (e.g., A2 carbonate-chert couplets, hot spring geyserite/terracettes, and channelized deposits), and then back to marine conditions (e.g., A3 jaspilitic chert)(Fig. 11). (B) Section 1S (the barite curl locality) preserves the transition from subaerial hot springs of A2 (e.g., Fe-rich shrub-like microbialites, geyserite, and sinter terracettes) to deeper water A3 jaspilitic chert. (C) Section 23S (The stromatolite creek locality) displays similar A1-A2 stratigraphy of section 16 N and is overlain by A4 volcaniclastic sandstone. These sections and their corresponding localities are detailed in Djokic et al., 2021.

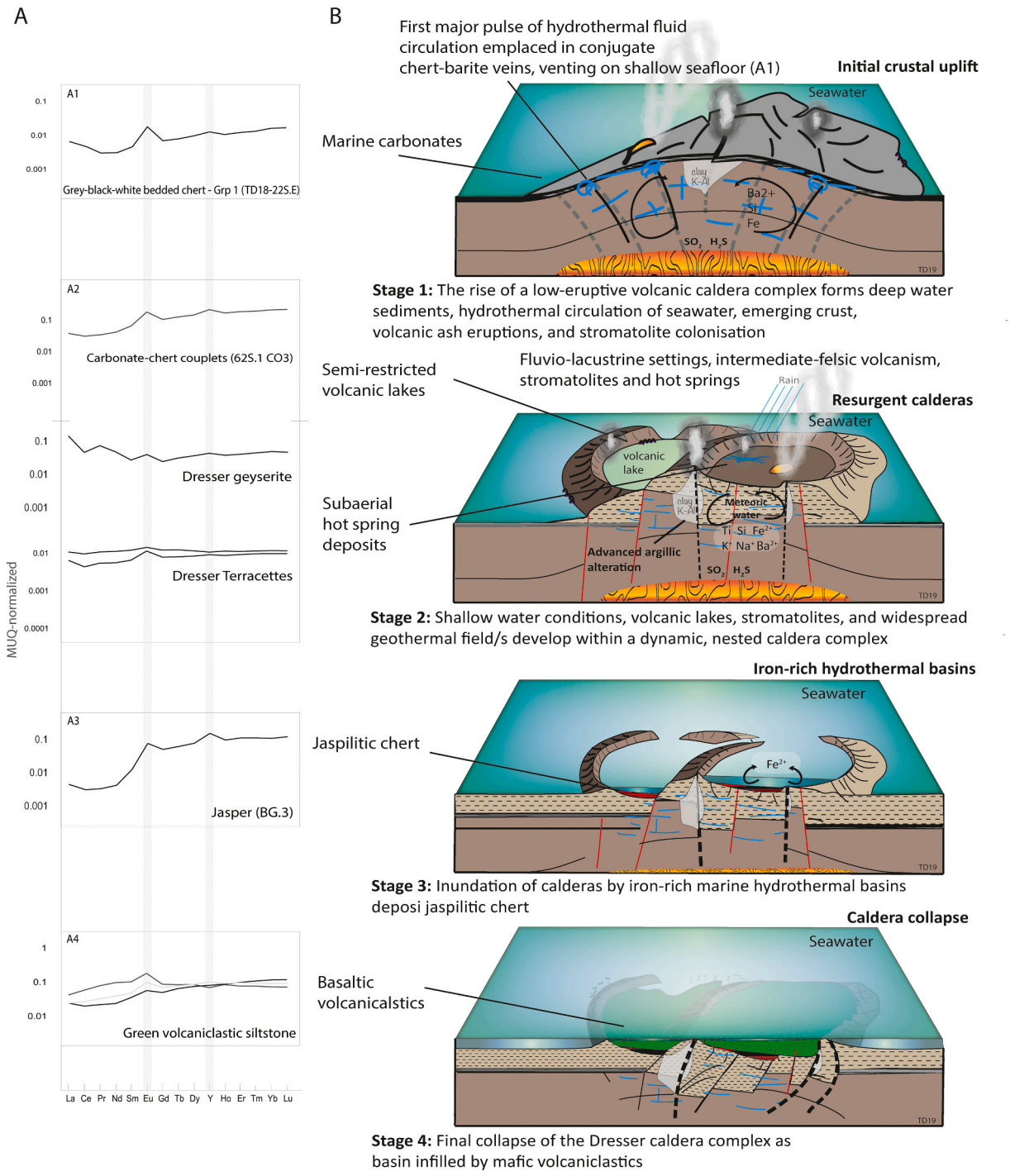


Fig. 12. Four-stage model illustrating the rise and fall of a low-eruptive volcanic caldera complex during deposition of DFc1 linked with REE + Y. (A) Representative REE + Y for precipitated rocks in assemblages 1–3 (A1-A3), and mafic volcaniclastic signatures of assemblage 4 (A4). (B) Stage 1: Initial crustal uplift caused by magmatic inflation. Deposition of deep-water sediments, intermediate-felsic ashes, breccias, and stromatolites during syngenetic emplacement of hydrothermal chert-barite veins. Stage 2: Nested calderas emerged above sea level allowing the formation of semi-restricted volcanic lakes, subaerial hot springs, and microbial communities. Stage 3: Subsiding calderas, allowed the inundation of seawater into hydrothermal caldera basins and the deposition of jaspilitic chert. Stage 4: Final caldera collapse caused by deflation of the underlying magma chamber. Erosion of caldera rocks (dominantly basalt) filling in basins.

from marine conditions (A1 bedded grey-black-white bedded chert) through to evaporative, hydrothermally-charged marine caldera lakes (A2 carbonate-chert couplets), to subaerial hot spring development and fluvial conditions (A2 geyserite and channelized deposits), and then back to deep water marine conditions (A3 jaspilitic chert) (Fig. 11A). The barite curl locality (1S) preserves the transition from subaerial hot springs of A2 (Fe-rich shrub-like microbialites, geyserite, and sinter terracettes: Djokic et al., 2017; Djokic et al., 2021) to deep marine conditions (A3 jaspilitic chert) (Fig. 11B). The 'stromatolite creek' locality (23S) displays the same A1-A2 stratigraphy of the geyserite locality (16 N), though is overlain by A4 basaltic conglomerate-sandstone-siltstone reflecting a transition from subaerial hot spring deposits to caldera collapse and basin infill (Fig. 11C; Fig. 12) (Van Kranendonk et al., 2008; Djokic, 2015).

This regression-transgression cycle, supplemented by REE + Y signatures, reflect changing fluid sources (marine, terrestrial, and/or low-high temperature hydrothermal) accompanying an evolving depositional environment (Fig. 12). These changes are interpreted to reflect a rise and fall of the crust relative to sea level (not sea level change), related to magmatic inflation (regression) and deflation (transgression) of the local land surface, during the evolution of a caldera system (Fig. 12) (Van Kranendonk, 2006; Van Kranendonk et al., 2008; Van Kranendonk et al., 2019 and references therein; Tadbiri and Van Kranendonk, 2020; Djokic et al., 2021).

Volcanic calderas may be marine, lacustrine, or terrestrial (subaerial) and consist of one or several (nested) calderas (Cole et al., 2005; Benson et al., 2017). Although Phanerozoic calderas commonly occur in extensional rift settings and produce peralkaline igneous rocks, they are known in basaltic settings on Earth and Mars (Cole et al., 2005; Wilson and Rowland, 2016). Calderas experience faulting and/or eruptive events, and low to high volumes of hydrothermal fluids including mixes of seawater, meteoric water, and/or magmatic fluids (Cole et al., 2005; Pirajno, 2009). Emergent/subaerial caldera basins can be distant from the sea such as Yellowstone National Park (Hurwitz and Lowenstern, 2014), or within volcanic islands restricted from, and/or open on one side to marine conditions such as the volcanic island of Niuafo'ou, Tonga (Kremer et al., 2012) and Satonda Crater Lake, Indonesia (Kempe and Kaźmierczak, 1993). Microbial communities (including stromatolites) thrive in volcanic caldera lakes and geothermal fields despite the volatility of these settings (Kempe and Kaźmierczak, 1993; Kaźmierczak and Kempe, 2006; Hurwitz and Lowenstern, 2014). Eruptions, ground-level inflation/collapse cycles, erosion, and faulting make calderas highly active depositional environments, resulting in complex structural collapse centers and rapid changes in the elevation of the caldera floor i.e., so-called piecemeal calderas (Cole et al., 2005). All of these criteria are present in DFc1, explaining its abruptly changing stratigraphy, abundant hydrothermal deposits, active growth faults, and variable REE + Y data (Fig. 12) (Nijman et al., 1998; Van Kranendonk and Pirajno, 2004; Van Kranendonk, 2006; Van Kranendonk et al., 2008; Van Kranendonk et al., 2019).

5.4. Evolution of the Dresser Formation volcanic caldera complex

REE + Y analyses presented here support deposition of DFc1 in four distinct caldera stages reflecting assemblages 1–4 (A-A4) (Fig. 12; Supp. Data 1; Djokic et al., 2021). These include the rise of a low-eruptive volcanic caldera, leading to felsic volcanism, crustal inflation, shallow water environments and stromatolites (stage 1); the development of emergent crust with widespread geothermal fields and volcanic lakes inhabited by microbial life (stage 2), iron-rich marine-hydrothermal basins (stage 3), and the final collapse of the Dresser caldera complex (stage 4) (Van Kranendonk, 2006; Van Kranendonk et al., 2008; Djokic et al., 2017; Van Kranendonk et al., 2019; Djokic et al., 2021; Johnson et al., 2022a; Johnson et al., 2022b). DFc1 may have deposited within a 13 ± 2 My period based on relative age dates of the underlying c. 3490 Ma North Star Basalt and overlying c. 3477 ± 2 Ma Duffer Formation (Thorpe, 1992; Van Kranendonk et al., 2002; Van Kranendonk, 2006; Van Kranendonk et al., 2008). This age range is comparable to Yellowstone National Park's volcanic lifespan (17 Ma), with individual calderas spanning ~1–3 million years, contributing to a complex volcanic-hydrothermal stratigraphy (Christiansen, 2001; Pierce and Morgan, 2009; Camp and Wells, 2021).

5.4.1. Stage 1: The rise of a low-eruptive volcanic caldera complex

The transition from basalt deposition to fossiliferous, chemical, and volcaniclastic sedimentary rocks of DFc1 was likely driven by crustal uplift, relative to sea level (Fig. 12: Stage 1), with evidence for a felsic-differentiated magmatic chamber (felsic tuffaceous rocks, A1 & A2) (Van Kranendonk et al., 2008; Djokic, 2015; Djokic et al., 2021). A low-eruptive piecemeal volcanic caldera accompanied extensive hydrothermal fluid flow (Nijman et al., 1998; Van Kranendonk, 2006; Van Kranendonk et al., 2008) through conjugate fracturing of the footwall (Tadbiri, 2018; Tadbiri and Van Kranendonk, 2020). This produced a complex stratigraphy of marine to shallow water deposits and volcaniclastic sedimentation including felsic volcaniclastic rocks, bedded grey-black-white chert, sandstone, and chert-barite breccia including stromatolites (Van Kranendonk et al., 2008; Djokic, 2020).

Although there is no clear evidence of subaerial deposits, the presence of local boulder conglomerate with jaspilitic chert, barite, and stromatolites in a felsic volcaniclastic matrix attests to the early onset of volcanic-hydrothermal processes and shallow-water environments. Notably, minor bedded jasper horizons indicate low-salinity terrestrial hydrothermal basins occurred during this time (Johnson et al., 2022a; Johnson et al., 2022b).

5.4.2. Stage 2: Shallow water conditions, volcanic lakes, stromatolites, and widespread geothermal field/s

This stage marks the establishment of a caldera complex with volcanic lakes, widespread geothermal field/s and diverse microbial communities (Fig. 12: Stage 2). The discontinuous, widespread distribution of the carbonate-chert unit ('zebra rock') associated with strongly sulfidized stromatolites implies shallow, wave-rippled volcanic lake shorelines were colonized by microbial communities (Van Kranendonk et al., 2008; Baumgartner et al., 2020a). Sulfide precipitation is known to occur in anoxygenic phototrophic hydrothermal microbial mats within Yellowstone National Park (Havig and Hamilton, 2019).

Geysers and hot spring pools/terraces formed alongside fluvial settings (channelized conglomerates interbedded with cross and flat laminated basaltic wacke i.e., green-red bedded chert; Section 5.2.1) (Djokic et al., 2017; Djokic, 2020; Djokic et al., 2021) and variable evolved basaltic-intermediate-felsic volcaniclastic sedimentation (grey-white bedded and massive grey chert units; see Section 5.2.1) (Van Kranendonk, 2006; Djokic et al., 2021).

Geochemical analysis of hot spring deposits and footwall basalt alteration suggest varied fluid chemistries (Van Kranendonk and Pirajno, 2004; Djokic et al., 2021). For example, Dresser geyserite and epithermal quartz veins point to the circulation of cool (120 °C), low-salinity (<3 wt% NaCl equiv.) geothermal fluids (Harris et al., 2009; Campbell et al., 2015), whereas tourmaline-bearing pyritic crusts with negative $\delta^{11}B$ values infer boron-bearing hot spring fluids (Ghosh et al., 2012; Steller et al., 2019; Van Kranendonk et al., 2019). The REE + Y of the Dresser terracettes (opal-carbonate sinter?) suggests another geothermal fluid chemistry (Section 5.2.1).

A diverse suite of inferred microbial structures is associated with the presumablyvaried hot spring fluid chemistries (Van Kranendonk et al., 2008; Stellar, 2016; Djokic et al., 2017; Djokic, 2020; Djokic et al., 2021). Indeed, a variety of stromatolite morphologies (wrinkly, wavy, domical, conical, elongate, pustular, columnar), microbialites (iron-shrubs), and microbialite-related fabrics (palisade, bubbles trapped in EPS) (Van Kranendonk et al., 2008; Djokic et al., 2017; Djokic et al., 2021) may have utilized chemosynthetic and/or photosynthetic (likely anoxygenic) metabolic regimes, typical of modern hot springs (Jones et al., 1998; Fouke et al., 2000; Stout et al., 2009; Ghosh et al., 2012; Campbell et al., 2015;Hamilton, 2019; Hamilton et al., 2019b).

Marine-influenced units such as bedded grey-black-white chert, flat laminated grey chert, and green-red bedded chert (Section 5.2.1), suggest the development of local caldera sub-basins that allowed temporary marine incursions. These could have been regularly inundated with seawater by the estimated 6 m-high tides that may have caused greater, more frequent, onshore-offshore interaction during shorter Archean days (e.g., Crawford et al., 2022). Many Recent and modern calderas persist at sea level and succumb to the relatively subdued modern tidal activity e.g., Santorini, Greece (Perissoratis, 1995), Aira caldera, Japan (Aramaki, 1984), Rabaul caldera, Papua New Guinea (Nairn et al., 1995), and Taal caldera, Philippines (Ramos, 2002).

These findings depict a complex volcanic-hydrothermal landscape,

where islands of nested calderas emerged and subsided into the sea. White Island in New Zealand, or the Phanerozoic Kerguelen Archipelago (Van Kranendonk and Pirajno, 2004; Djokic, 2015), may serve as relevant present-day analogs.

5.4.3. Stage 3: Iron-rich hydrothermal basins

A shift from Stage 2 subaerial deposits to Stage 3 deep-marine-hydrothermal conditions is marked by discontinuous, fault-controlled lenses of Jaspilitic chert in DFc1 structural blocks (Fig. 12: Stage 3) (Djokic, 2015; Johnson et al., 2022a; Johnson et al., 2022b). The absence of stromatolites supports deposition under deep-water conditions below the photic zone. Rapid deposition within a deepening basin may be why the thin hot spring deposits are preserved, as is suggested for the preservation of geothermal (and other delicate) deposits worldwide (e.g., Christiansen, 2001; Guido and Campbell, 2011 and references therein). Subdued hydrothermal fluid circulation evidenced by a low volume of chert-barite veining, suggests initial caldera subsidence via permanent inundation of seawater into the caldera(s) (Tadbiri, 2018; Tadbiri and Van Kranendonk, 2020).

5.4.4. Stage 4: Final collapse of the Dresser caldera complex

This final depositional stage reflects rapid basin subsidence and clastic infill (Fig. 12: Stage 4) (Van Kranendonk and Pirajno, 2004; Djokic, 2015). Basin subsidence is highlighted by a large growth-fault-controlled sedimentary wedge, north of the Dresser Mine, filled by tens of meters of green volcaniclastic conglomerate-sandstone-siltstone (Section 5.2.3) (Poole, 2013; Djokic, 2015; Tadbiri, 2018; Djokic, 2020: see sites 1N - 21N Supp. Fig. 4.1; Tadbiri and Van Kranendonk, 2020). Major listric growth faults are identified as the final vein set, which extends to the tops of the Dresser Formation and represents asymmetric 'trapdoor-type' collapse of caldera floor segments (Tadbiri, 2018; Tadbiri and Van Kranendonk, 2020). Collapse may have been triggered by a large tuff-forming eruption that is not preserved. Volcanic ash can disperse tens of kilometers away from an eruptive center and if any such eruption occurred the remnant unit is not intersected by the portion of Dresser Formation exposed. The absence of stromatolites and presence of cross-cutting quartz-sulfide veins suggest several hundred meters of basin depth where sunlight did not penetrate and hydrothermal fluids did not boil (Buchanan, 1981; Van Kranendonk and Pirajno, 2004; Poole, 2013). Some periods of low clastic input are indicated by minor marine-hydrothermal jaspers (Johnson et al., 2022a; Johnson et al., 2022b). Subsequent to A4, extrusion of basalt filled the remaining areas of the caldera (Fig. 1), marking the end of this early life habitat.

6. Conclusions

Integrated datasets are required to accurately reconstruct and develop holistic depositional models of early life sites such as the Dresser Formation lower chert-barite sequence (DFc1). These datasets must include investigation of regional and lithostratigraphic successions, local lithofacies variations, sedimentology, hydrothermal veins, hydrothermal alteration, structural geology, and geochemistry. Here we provide evidence from variations in REE + Y geochemistry linked with lithostratigraphy to demonstrate that DFc1 deposited across a transition from deep marine to shallow-water (A1) to subaerial (A2), and back to marine (A3-A4) conditions. Evaporative lacustrine, fluvial, and terrestrial hot spring deposits developed during a period of emerged crust, when life flourished. REE + Y helped to characterize protoliths and trace fluid sources of terrestrial hot spring deposits, seawater signatures, hydrothermal fluids, and igneous input. These findings highlight the complex nature and evolution of the Dresser Formation caldera system, based on similarities with modern hydrothermal systems. This provides context for early life and informs the search for life on Mars and origin of life studies.

Supplementary data to this article can be found online at https://doi.org/10.1016/j.chemgeo.2023.121865.

CRediT authorship contribution statement

T. Djokic: Conceptualization, Data curation, Formal analysis, Investigation, Methodology, Visualization, Writing – original draft, Writing – review & editing. **R. Bolhar:** Visualization, Writing – review & editing, Formal analysis. **L.A. Brengman:** Formal analysis, Methodology, Writing – review & editing. **J.R. Havig:** Formal analysis, Methodology, Writing – review & editing. **M.J. Van Kranendonk:** Conceptualization, Formal analysis, Investigation, Supervision, Writing – review & editing.

Declaration of Competing Interest

None.

Data availability

Data will be made available on request.

Acknowledgements

We acknowledge the Nyamal peoples as the traditional custodians of the land on which we conducted field work. The authors give thanks to A. Greig for trace element analyses, Mark van Zuilen for providing insights on drillcore data, Clark Johnson for discussion which greatly improved the quality of this manuscript, and Ross Pogson for mineralogical discussion. Faye and Geoff Myers, and Haoma Mining Pty Ltd. provided hospitality and support on site at the Dresser Formation. This research was funded by Australian Research Council Discovery Project DP180103204 to MVK; Australian Government Research Training Program Scholarship to T.D. We also thank the reviewers, who greatly helped to improve the quality of this work and M. Fiorentini for editorial handling.

References

Akagi, T., 2013. Rare earth element (REE)–silicic acid complexes in seawater to explain the incorporation of REEs in opal and the "leftover" REEs in surface water: new interpretation of dissolved REE distribution profiles. Geochim. Cosmochim. Acta 113, 174–192.

Alibert, C., McCulloch, M.T., 1993. Rare earth element and neodymium isotopic compositions of the banded iron-formations and associated shales from Hamersley, Western Australia. Geochim. Cosmochim. Acta 57 (1), 187–204.

Allwood, A.C., Kamber, B.S., Walter, M.R., Burch, I.W., Kanik, I., 2010. Trace elements record depositional history of an early Archean stromatolitic carbonate platform. Chem. Geol. 270 (1–4), 148–163.

Aramaki, S., 1984. Formation of the Aira caldera, southern Kyushu,~ 22,000 years ago. J. Geophys. Res. Solid Earth 89 (B10), 8485–8501.

Babechuk, M.G., Kamber, B.S., Greig, A., Canil, D., Kodolányi, J., 2010. The behaviour of tungsten during mantle melting revisited with implications for planetary differentiation time scales. Geochim. Cosmochim. Acta 74 (4), 1448–1470.

Baldwin, G.J., Thurston, P.C., Kamber, B.S., 2011. High-precision rare earth element, nickel, and chromium chemistry of chert microbands pre-screened with in-situ analysis. Chem. Geol. 285 (1–4), 133–143.

Bao, S.-X., Zhou, H.-Y., Peng, X.-T., Ji, F.-W., Yao, H.-Q., 2008. Geochemistry of REE and yttrium in hydrothermal fluids from the Endeavour segment, Juan de Fuca Ridge. Geochem. J. 42 (4), 359–370.

Barley, M.E., Dunlop, J.S.R., Glover, J.E., Groves, D.I., 1979. Sedimentary evidence for an Archaean shallow-water volcanic-sedimentary facies, eastern Pilbara Block, Western Australia. Earth Planet. Sci. Lett. 43 (1), 74–84.

Barrat, J.A., Boulegue, J., Tiercelin, J.J., Lesourd, M., 1999. Strontium isotopes and rare-earth element geochemistry of hydrothermal carbonate deposits from Lake Tanganyika, East Africa. Geochim. Cosmochim. Acta 64 (2), 287–298.

Bau, M., 1996. Controls on the fractionation of isovalent trace elements in magmatic and aqueous systems: evidence from Y/Ho, Zr/Hf, and lanthanide tetrad effect. Contrib. Mineral. Petrol. 123 (3), 323–333.

Bau, M., Dulski, P., 1996. Distribution of yttrium and rare-earth elements in the Penge and Kuruman iron-formations, Transvaal Supergroup, South Africa. Precambrian Res. 79 (1–2), 37–55.

Baumgartner, R.J., et al., 2019. Nano-porous pyrite and organic matter in 3.5-billion-year-old stromatolites record primordial life. Geology 47 (11), 1039–1043.

Baumgartner, R.J., et al., 2020a. Sulfidization of 3.48 billion-year-old stromatolites of the Dresser Formation, Pilbara Craton: Constraints from in-situ sulfur isotope analysis of pyrite. Chem. Geol. 538, 119488.

Baumgartner, R.J., et al., 2020b. Formation of micro-spherulitic barite in association with organic matter within sulfidized stromatolites of the 3.48 billion-year-old Dresser Formation, Pilbara Craton. Geobiology 18 (4), 415–425.
Baumgartner, R.J., et al., 2020c. Accumulation of transition metals and metalloids in sulfidized stromatolites of the 3.48 Billion–year–old Dresser Formation, Pilbara Craton. Precambrian Res. 337 (105534).
Benson, T.R., Mahood, G.A., Grove, M., 2017. Geology and 40Ar/39Ar geochronology of the middle Miocene McDermitt volcanic field, Oregon and Nevada: Silicic volcanism associated with propagating flood basalt dikes at initiation of the Yellowstone hotspot. Geol. Soc. Am. Bull. 129 (9–10), 1027–1051.
Bertram, C.J., Elderfield, H., 1993. The geochemical balance of the rare earth elements and neodymium isotopes in the oceans. Geochim. Cosmochim. Acta 57 (9), 1957–1986.
Bilal, B.A., 1991. Thermodynamic study of Eu3+/Eu2+ redox reaction in aqueous solutions at elevated temperatures and pressures by means of cyclic voltammetry. Zeitschrift für Naturforschung A 46 (12), 1108–1116.
Bolhar, R., Kamber, B.S., Moorbath, S., Fedo, C.M., Whitehouse, M.J., 2004. Characterisation of early Archaean chemical sediments by trace element signatures. Earth Planet. Sci. Lett. 222 (1), 43–60.
Bolhar, R., Van Kranendonk, M.J., Kamber, B.S., 2005. A trace element study of siderite–jasper banded iron formation in the 3.45 Ga Warrawoona Group, Pilbara Craton—formation from hydrothermal fluids and shallow seawater. Precambrian Res. 137 (1), 93–114.
Bolhar, R., Hofmann, A., Siahi, M., Feng, Y.-X., Delvigne, C., 2015. A trace element and Pb isotopic investigation into the provenance and deposition of stromatolitic carbonates, ironstones and associated shales of the~ 3.0 Ga Pongola Supergroup, Kaapvaal Craton. Geochim. Cosmochim. Acta 158, 57–78.
Brasier, M.D., Antcliffe, J., Saunders, M., Wacey, D., 2015. Changing the picture of Earth's earliest fossils (3.5–1.9 Ga) with new approaches and new discoveries. Proceedings of the National Academy of Sciences 112, 4859–4864.
Brasier, M.D., Green, O.R., Jephcoat, A.P., Kleppe, A.K., Van Kranendonk, M.J., Lindsay, J.F., Steele, A., Grassineau, N.V., 2002. Questioning the evidence for Earth's oldest fossils. Nature 416, 76–81.
Brasier, M., Green, O., Lindsay, J., Steele, A., 2004. Earth's Oldest (~ 3.5 Ga) Fossils and theEarly Eden Hypothesis': Questioning the Evidence. Origins of Life and Evolution of the Biosphere 34, 257–269.
Brengman, L.A., Fedo, C.M., 2018. Development of a mixed seawater-hydrothermal fluid geochemical signature during alteration of volcanic rocks in the Archean (~ 2.7 Ga) Abitibi Greenstone Belt, Canada. Geochim. Cosmochim. Acta 227, 227–245.
Buchanan, L.J., 1981. Precious metal deposits associated with volcanic environments in the southwest. Geol. Soc. Arizona Digest 14, 237–262.
Buick, R., 1985. Life and Conditions in the Early Archaean: Evidence from 3500 M.Y. Old Shallow-Water Sediments in the Warrawoon Group. North Pole, Western Australia, The University of Western Australia.
Buick, R., Barnes, K., 1984. Cherts in the Warrawoona Group: Early Archaean Silicified Sediments Deposited in Shallow-water Environments, 9. University of Western Australia, Geological Department & University Extension, Publication, pp. 37–53.
Buick, R., Dunlop, J.S.R., 1990. Evaporitic sediments of early Archaean age from the Warrawoona Group, North Pole, Western Australia. Sedimentology 37 (2), 247–277.
Camp, V.E., Wells, R., 2021. The case for a long-lived and robust Yellowstone hotspot. GSA Today 31 (1), 4–10.
Campbell, K.A., Rodgers, K., Brotheridge, J.M., Browne, P., 2002. An unusual modern silica–carbonate sinter from Pavlova spring, Ngatamariki, New Zealand. Sedimentology 49 (4), 835–854.
Campbell, K.A., et al., 2015. Geyserite in hot-spring siliceous sinter: Window on Earth's hottest terrestrial (paleo) environment and its extreme life. Earth Sci. Rev. 148, 44–64.
Canet, C., et al., 2005. Silica-carbonate stromatolites related to coastal hydrothermal venting in Bahía Concepción, Baja California Sur, Mexico. Sediment. Geol. 174 (1), 97–113.
Caruso, S., Van Kranendonk, M.J., Baumgartner, R.J., Fiorentini, M.L., Forster, M.A., 2021. The role of magmatic fluids in the~ 3.48 Ga Dresser Caldera, Pilbara Craton: New insights from the geochemical investigation of hydrothermal alteration. Precambrian Res. 362, 106299.
Caruso, S., Baumgartner, R.J., Van Kranendonk, M.J., Fiorentini, M.L., Dosseto, A., 2023. The mobilization of boron and lithium in the hydrothermal system of the~ 3.48 Ga Dresser caldera: a stable isotope perspective. Chem. Geol. 616, 121232.
Christiansen, R.L., 2001. The Quaternary and Pliocene Yellowstone Plateau volcanic field of Wyoming, Idaho, and Montana. 729G, USGS.
Cole, J.W., Milner, D.M., Spinks, K.D., 2005. Calderas and caldera structures: a review. Earth Sci. Rev. 69 (1), 1–26.
Cox, K.G., Pankhurst, R.J., Bell, J.D., 1984. The Interpretation of Igneous Rocks. G. Allen & Unwin, Sydney.
Crawford, E.B., Arbic, B.K., Sheldon, N.D., Ansong, J.K., Timko, P.G., 2022. Investigating the behavior of mid-Archean tides and potential implications for biogeochemical cycling. Precambrian Res. 380, 106799.
De Baar, H.J.W., Brewer, P.G., Bacon, M.P., 1985. Anomalies in rare earth distributions in seawater: Gd and Tb. Geochim. Cosmochim. Acta 49 (9), 1961–1969.
Dekov, V., et al., 2014. Hydrothermal carbonate chimneys from a continental rift (Afar Rift): mineralogy, geochemistry, and mode of formation. Chem. Geol. 387, 87–100.
Dekov, V.M., et al., 2015. Geochemistry and mineralogy of a silica chimney from an inactive seafloor hydrothermal field (East Pacific rise, 18° S). Chem. Geol. 415, 126–140.
Djokic, T., 2015. Assessing the Link between Earth's Earliest Convincing Evidence of Life and Hydrothermal Fluids: The c. 3.5 Ga Dresser Formation of the North Pole Dome, Pilbara Craton. The University of New South Wales, Western Australia, p. 158.
Djokic, T., 2020. Lithofacies and Biofacies Analysis of Earth's Oldest Subaerial Hot Spring Deposits from the Ca. 3.5 Ga Dresser Formation, Pilbara Craton. The University of New South Wales, Western Australia, p. 309.
Djokic, T., Van Kranendonk, M.J., 2018. Textural biosignatures from the Pilbara: an important benchmark for early life on Earth. PalZ 92 (2), 191–193.
Djokic, T., Van Kranendonk, M.J., Campbell, K.A., Walter, M.R., Ward, C.R., 2017. Earliest signs of life on land preserved in ca. 3.5 Ga hot spring deposits. Nat. Commun. 8, 15263.
Djokic, T., et al., 2021. A reconstructed subaerial hot spring field in the ~3.5 billion-year-old Dresser Formation, North Pole Dome, Pilbara Craton, Western Australia. Astrobiology 20 (9).
Douville, E., et al., 1999. Yttrium and rare earth elements in fluids from various deep-sea hydrothermal systems. Geochim. Cosmochim. Acta 63 (5), 627–643.
Duda, J.-P., et al., 2018. Ideas and perspectives: hydrothermally driven redistribution and sequestration of early Archaean biomass–the "hydrothermal pump hypothesis". Biogeosciences 15 (5), 1535–1548.
Dunlop, J., Milne, V., Groves, D., Muir, M., 1978. A new microfossil assemblage from the Archaean of Western Australia. Nature 274 (5672), 676–678.
Eggins, S.M., et al., 1997. A simple method for the precise determination of≥ 40 trace elements in geological samples by ICPMS using enriched isotope internal standardisation. Chem. Geol. 134 (4), 311–326.
Elderfield, H.J., 1988. The oceanic chemistry of the rare-earth elements. Philos. Trans. R. Soc. 325 (1583), 105–126.
Ewers, G.R., Wood, D.G., Tedder, I.J., Haas, L., Hoffman, C.F., 1992. Epithermal gold mineralisation in the northern Drummond Basin, Queensland. Austral. Geol. Surv. Organis. Miner. Land Use Progr. Record 1992 (72), 67.
Feng, J.-L., Zhao, Z.-H., Chen, F., Hu, H.-P., 2014. Rare earth elements in sinters from the geothermal waters (hot springs) on the Tibetan Plateau, China. J. Volcanol. Geotherm. Res. 287, 1–11.
Fouke, B.W., et al., 2000. Depositional facies and aqueous-solid geochemistry of travertine-depositing Hot Springs (Angel Terrace, Mammoth Hot Springs, Yellowstone National Park, USA). J. Sediment. Res. 70 (3), 565–585.
Frimmel, H.E., 2009. Trace element distribution in Neoproterozoic carbonates as palaeoenvironmental indicator. Chem. Geol. 258 (3–4), 338–353.
Ghosh, W., et al., 2012. Molecular and cellular fossils of a mat-like microbial community in geothermal boratic sinters. Geomicrobiol J. 29 (10), 879–885.
Glikson, M., et al., 2008. Microbial remains in some earliest Earth rocks: comparison with a potential modern analogue. Precambrian Res. 164 (3), 187–200.
Goldberg, E.D., 1954. Marine geochemistry 1. Chemical scavengers of the sea. J. Geol. 62 (3), 249–265.
Greaves, M., Elderfield, H., Sholkovitz, E., 1999. Aeolian sources of rare earth elements to the Western Pacific Ocean. Mar. Chem. 68 (1–2), 31–38.
Groves, D.I., Dunlop, J.S.R., Buick, R., 1981. An early habitat of life. Sci. Am. 245, 64–73.
Guido, D.M., Campbell, K.A., 2011. Jurassic hot spring deposits of the Deseado Massif (Patagonia, Argentina): characteristics and controls on regional distribution. J. Volcanol. Geotherm. Res. 203 (1–2), 35–47.
Guidry, S.A., Chafetz, H.S., 2003. Anatomy of siliceous hot springs: examples from Yellowstone National Park, Wyoming, USA. Sediment. Geol. 157 (1–2), 71–106.
Hamilton, T.L., 2019. The trouble with oxygen: the ecophysiology of extant phototrophs and implications for the evolution of oxygenic photosynthesis. Free Radic. Biol. 140, 233–249.
Hamilton, A.R., Campbell, K.A., Rowland, J.V., Barker, S., Guido, D.M., 2019a. Fossilised geothermal surface features of the Whitianga Volcanic Centre (Miocene), Coromandel Volcanic Zone, New Zealand: controls and characteristics. J. Volcanol. Geotherm. Res. 381, 209–226.
Hamilton, T.L., Bennett, A.C., Murugapiran, S.K., Havig, J.R., 2019b. Anoxygenic phototrophs span geochemical gradients and diverse morphologies in terrestrial geothermal springs. Msystems 4 (6). https://doi.org/10.1128/msystems.00498-19.
Harris, A.C., et al., 2009. Early Archean hot springs above epithermal veins, North Pole, Western Australia: new insights from fluid inclusion microanalysis. Econ. Geol. 104 (6), 793–814.
Havig, J.R., Hamilton, T.L., 2019. Productivity and community composition of low biomass/high silica precipitation hot springs: a possible window to earth's early biosphere? Life 9 (3), 64.
Hickman, A.H., Van Kranendonk, M.J., 2012. Early Earth evolution: evidence from the 3.5-1.8 Ga geological history of the Pilbara region of Western Australia. Episodes 35, 284–297.
Hickman-Lewis, K., et al., 2022. Advanced two-and three-dimensional insights into Earth's oldest stromatolites (ca. 3.5 Ga): prospects for the search for life on Mars. Geology 51 (1), 33–38.
Hofmann, A., Bolhar, R., Orberger, B., Foucher, F., 2013. Cherts of the Barberton Greenstone Belt, South Africa: Petrology and trace-element geochemistry of 3.5 to 3.3 Ga old silicified volcaniclastic sediments. S. Afr. J. Geol. 116 (2), 297–322.
Hollings, P., Kerrich, R., 2000. An Archean arc basalt–Nb-enriched basalt–adakite association: the 2.7 Ga Confederation assemblage of the Birch–Uchi greenstone belt, Superior Province. Contrib. Mineral. Petrol. 139 (2), 208–226.
Hopf, S., 1993. Behaviour of rare earth elements in geothermal systems of New Zealand. J. Geochem. Explor. 47 (1–3), 333–357.
Hurwitz, S., Lowenstern, J.B., 2014. Dynamics of the Yellowstone hydrothermal system. Rev. Geophys. 52 (3), 375–411.
Johannesson, K.H., Cortés, A., Ramos Leal, J.A., Ramírez, A.G., Durazo, J., 2005. Geochemistry of rare earth elements in groundwaters from a rhyolite aquifer, Central México. Rare Earth Elements Groundwater Flow Systems 187–222.
Johnson, C.M., et al., 2022a. Early Archean biogeochemical iron cycling and nutrient availability: new insights from a 3.5 Ga land-sea transition. Earth Sci. Rev. 228, 103992.

Johnson, C.M., et al., 2022b. Reply to comment by Birger Rasmussen and Janet R. Muhling on "Early Archean biogeochemical iron cycling and nutrient availability: New insights from a 3.5 Ga land-sea transition" by Johnson et al. Earth Sci. Rev. 231, 104087.
Jones, B., Renaut, R.W., Rosen, M.R., 1998. Microbial biofacies in hot-spring sinters: a model based on Ohaaki Pool, North Island, New Zealand. J. Sediment. Res. 68 (3).
Kamber, B.S., Webb, G.E., 2001. The geochemistry of late Archaean microbial carbonate: implications for ocean chemistry and continental erosion history. Geochim. Cosmochim. Acta 65 (15), 2509–2525.
Kamber, B.S., Greig, A., Schoenberg, R., Collerson, K.D., 2003. A refined solution to Earth's hidden niobium: implications for evolution of continental crust and mode of core formation. Precambrian Res. 126 (3–4), 289–308.
Kamber, B.S., Greig, A., Collerson, K.D., 2005. A new estimate for the composition of weathered young upper continental crust from alluvial sediments, Queensland, Australia. Geochim. Cosmochim. Acta 69 (4), 1041–1058.
Kaźmierczak, J., Kempe, S., 2006. Genuine modern analogues of Precambrian stromatolites from caldera lakes of Niuafo'ou Island, Tonga. Naturwissenschaften 93 (3), 119–126.
Kempe, S., Kaźmierczak, J., 1993. Satonda Crater Lake, Indonesia: hydrogeochemistry and biocarbonates. Facies 28 (1), 1–31.
Kim, K.-H., Byrne, R.H., Lee, J.H., 1991. Gadolinium behavior in seawater: a molecular basis for gadolinium anomalies. Mar. Chem. 36 (1–4), 107–120.
Kremer, B., Kazmierczak, J., Łukomska-Kowalczyk, M., Kempe, S., 2012. Calcification and silicification: Fossilization potential of cyanobacteria from stromatolites of Niuafo 'ou's Caldera Lakes (Tonga) and implications for the early fossil record. Astrobiology 12 (6), 535–548.
Lee, J.H., Byrne, R.H., 1992. Complexation of trivalent rare earth elements (Ce, Eu, Gd, Tb, Yb) by carbonate ions. Geochim. Cosmochim. Acta 57 (2), 295–302.
Lewis, A.J., Palmer, M.R., Sturchio, N.C., Kemp, A.J., 1997. The rare earth element geochemistry of acid-sulphate and acid-sulphate-chloride geothermal systems from Yellowstone National Park, Wyoming, USA. Geochim. Cosmochim. Acta 61 (4), 695–706.
Lewis, A., Komninou, A., Yardley, B., Palmer, M., 1998. Rare earth element speciation in geothermal fluids from Yellowstone National Park, Wyoming, USA. Geochim. Cosmochim. Acta 62 (4), 657–663.
Lindsay, J.F., et al., 2005. The problem of deep carbon—an Archean paradox. Precambrian Res. 143 (1–4), 1–22.
Liu, L., Ireland, T., Holden, P., 2021. SHRIMP 4-S Isotope Systematics of Two Pyrite Generations in the 3.49 Ga Dresser Formation.
Lowe, D.R., 1994. Abiological origin of described stromatolites older than 3.2 Ga. Geology 22, 387–390.
MacRae, N.D., Nesbitt, H.W., Kronberg, B.I., 1992. Development of a positive Eu anomaly during diagenesis. Earth Planet. Sci. Lett. 109 (3–4), 585–591.
Maliva, R.G., Knoll, A.H., Simonson, B.M., 2005. Secular change in the Precambrian silica cycle: insights from chert petrology. Geol. Soc. Am. Bull. 117 (7–8), 835–845.
Martin, H., Smithies, R.H., Rapp, R., Moyen, J.-F., Champion, D., 2005. An overview of adakite, tonalite–trondhjemite–granodiorite (TTG), and sanukitoid: relationships and some implications for crustal evolution. Lithos 79 (1–2), 1–24.
McCarthy, K.T., Pichler, T., Price, R.E., 2005. Geochemistry of Champagne Hot Springs shallow hydrothermal vent field and associated sediments, Dominica, Lesser Antilles. Chem. Geol. 224, 55–68.
McDonough, W.F., Sun, S.-S., 1995. The composition of the Earth. Chem. Geol. 120 (3–4), 223–253.
McLennan, S.M., 1989. Rare earth elements in sedimentary rocks: influence of provenance and sedimentary processes. In: Geochemistry and Mineralogy of Rare Earth Elements, Reviews in Mineralogy, 21, pp. 169–200.
McLoughlin, N., Wilson, L.A., Brasier, M.D., 2008. Growth of synthetic stromatolites and wrinkle structures in the absence of microbes–implications for the early fossil record. Geobiology 6, 95–105.
Michard, A., 1989. Rare earth element systematics in hydrothermal fluids. Geochim. Cosmochim. Acta 53 (3), 745–750.
Mielke, J., 1979. Composition of the Earth's crust and distribution of the elements. In: Review of research on modern problems in geochemistry. UNESCO Report, Paris, pp. 9–37.
Mills, R.A., Elderfield, H., 1995. Rare earth element geochemistry of hydrothermal deposits from the active TAG Mound, 26 N Mid-Atlantic Ridge. Geochim. Cosmochim. Acta 59 (17), 3511–3524.
Morag, N., et al., 2016. Microstructure-specific carbon isotopic signatures of organic matter from~ 3.5 Ga cherts of the Pilbara Craton support a biologic origin. Precambrian Res. 275, 429–449.
Muller, É., Philippot, P., Rollion-Bard, C., Cartigny, P., 2016. Multiple sulfur-isotope signatures in Archean sulfates and their implications for the chemistry and dynamics of the early atmosphere. Proc. Natl. Acad. Sci. 113 (27), 7432–7437.
Murray, R.W., Ten Brink, M.R.B., Gerlach, D.C., Russ III, G.P., Jones, D.L., 1991. Rare earth, major, and trace elements in chert from the Franciscan complex and Monterey Group, California: assessing REE sources to fine-grained marine sediments. Geochim. Cosmochim. Acta 55 (7), 1875–1895.
Nairn, I., McKee, C., Talai, B., Wood, C., 1995. Geology and eruptive history of the Rabaul Caldera area, Papua New Guinea. J. Volcanol. Geotherm. Res. 69 (3–4), 255–284.
Nijman, W., de Bruijne, K.C.H., Valkering, M.E., 1998. Growth fault control of early Archaean cherts, barite mounds and chert-barite veins, North Pole Dome, Eastern Pilbara, Western Australia. Precambrian Res. 88 (1–4), 25–52.
Noffke, N., Christian, D., Wacey, D., Hazen, R.M., 2013. Microbially induced sedimentary structures recording an ancient ecosystem in the ca. 3.48 billion-year-old Dresser Formation, Pilbara, Western Australia. Astrobiology 13 (12), 1103–1124.
Nozaki, Y., Zhang, J., Amakawa, H., 1997. The fractionation between Y and Ho in the marine environment. Earth Planet. Sci. Lett. 148 (1–2), 329–340.
Olivier, N., Boyet, M., 2006. Rare earth and trace elements of microbialites in Upper Jurassic coral-and sponge-microbialite reefs. Chem. Geol. 230 (1–2), 105–123.
Otálora, F., et al., 2018. A crystallographic study of crystalline casts and pseudomorphs from the 3.5 Ga Dresser Formation, Pilbara Craton (Australia). J. Appl. Crystallogr. 51, 1050–1058.
Perissoratis, C., 1995. The Santorini volcanic complex and its relation to the stratigraphy and structure of the Aegean arc, Greece. Mar. Geol. 128 (1–2), 37–58.
Philippot, P., et al., 2007. Early Archaean microorganisms preferred elemental sulfur, not sulfate. Science 317 (5844), 1534–1537.
Piepgras, D.J., Jacobsen, S.B., 1992. The behavior of rare earth elements in seawater: Precise determination of variations in the North Pacific water column. Geochim. Cosmochim. Acta 56 (5), 1851–1862.
Pierce, K.L., Morgan, L.A., 2009. Is the track of the Yellowstone hotspot driven by a deep mantle plume?—Review of volcanism, faulting, and uplift in light of new data. J. Volcanol. Geotherm. Res. 188 (1–3), 1–25.
Pirajno, F., 2009. Hydrothermal Processes and Mineral Systems. Springer.
Planavsky, N.J., Robbins, L.J., Kamber, B.S., Schoenberg, R., 2020. Weathering, alteration and reconstructing Earth's oxygenation. Interf. Focus 10 (4), 20190140.
Poole, G., 2013. Modeling Hydrothermal Alteration Facies of Earth's Oldest Hydrothermal Setting: The 3.5 Ga North Pole Dome. University of New South Wales, Western Australia, Australia, p. 85.
Prakash, L.S., et al., 2012. Distribution of REEs and yttrium among major geochemical phases of marine Fe–Mn-oxides: Comparative study between hydrogenous and hydrothermal deposits. Chem. Geol. 312, 127–137.
Ramos, E.G., 2002. Origin and geologic features of Taal Lake, Philippines. Aquat. Ecosyst. Health Manag. 5 (2), 155–162.
Renaut, R.W., Jones, B., 1997. Controls on aragonite and calcite precipitation in hot spring travertines at Chemurkeu, Lake Bogoria, Kenya. Can. J. Earth Sci. 34 (6), 801–818.
Rividi, N., 2010. Diagenesis and Hydrothermalism of Archean Oceanic Sediments (3,5 Gyr, Dresser Formation, Pilbara Craton, Australia): A Window on Early Terrestrial Ecosystems, Université Denis Diderot, Paris 7, Paris, p. 244.
Shen, Y., Buick, R., Canfield, D.E., 2001. Isotopic evidence for microbial sulphate reduction in the early Archaean era. Nature 410 (6824), 77.
Shen, Y., Farquhar, J., Masterson, A., Kaufman, A.J., Buick, R., 2009. Evaluating the role of microbial sulfate reduction in the early Archean using quadruple isotope systematics. Earth Planet. Sci. Lett. 279 (3), 383–391.
Sholkovitz, E.R., Landing, W.M., Lewis, B.L., 1994. Ocean particle chemistry: the fractionation of rare earth elements between suspended particles and seawater. Geochim. Cosmochim. Acta 58 (6), 1567–1579.
Siever, R., 1992. The silica cycle in the Precambrian. Geochim. Cosmochim. Acta 56 (8), 3265–3272.
Smithies, R., Champion, D., Van Kranendonk, M., Hickman, A., 2007. Geochemistry of Volcanic Rocks of the Northern Pilbara Craton, Western Australia. Geological Survey of Western Australia Report, p. 104.
Smithies, R.H., Champion, D.C., Van Kranendonk, M.J., 2019. The oldest well-preserved felsic volcanic rocks on Earth: Geochemical clues to the early evolution of the Pilbara supergroup and implications for the growth of Paleoarchean Protocontinent. In: Van Kranendonk, M.J., Bennett, V., Hoffmann, E. (Eds.), In: Earth's Oldest Rocks. Elsevier, Netherlands, pp. 463–484.
Stellar, L., 2016. Origin of Boron in Hot Spring Deposits of the 3.48 Ga Dresser Formation, Pilbara Craton: Insights from Modern Analogues in India and Indonesia. Honours Thesis. University of New South Wales, p. 23.
Steller, L.H., et al., 2019. Boron Isotopes in the Puga Geothermal System, India, and their Implications for the Habitat of early Life. Astrobiology 19 (12), 1459–1473.
Stout, L.M., Blake, R.E., Greenwood, J.P., Martini, A.M., Rose, E.C., 2009. Microbial diversity of boron-rich volcanic hot springs of St. Lucia, Lesser Antilles. FEMS Microbiol. Ecol. 70 (3), 402–412.
Sveinbjornsdottir, A.E., Coleman, M.L., Yardley, B.W.D., 1986. Origin and history of hydrothermal fluids of the Reykjanes and Krafla geothermal fields, Iceland. Contrib. Mineral. Petrol. 94 (1), 99–109.
Tadbiri, S., 2018. Structural and Kinematic Analysis of the 3.5 Ga Hydrothermal Chert-Barite Vein Network of the Stromatolitic Dresser Formation, North Pole Dome, Western Australia. The University of New South Wales, p. 172.
Tadbiri, S., Van Kranendonk, M.J., 2020. Structural analysis of syn-depositional hydrothermal veins of the 3.48 Ga Dresser Formation, Pilbara Craton, Australia. Precambrian Res. 347, 105844.
Teboul, P.-A., et al., 2016. Origins of elements building travertine and tufa: New perspectives provided by isotopic and geochemical tracers. Sediment. Geol. 334, 97–114.
Thorpe, R., 1992. Constraints to Models for Lead Evolution from Precise Zircon U-Pb Geochronology for the Marble Bar region, Pilbara Craton, Western Australia, 9. The Archaean: Terrains, Processes and Metallogeny Publication, pp. 395–406.
Tostevin, R., et al., 2016. Effective use of cerium anomalies as a redox proxy in carbonate-dominated marine settings. Chem. Geol. 438, 146–162.
Ueno, Y., Isozaki, Y., Yurimoto, H., Maruyama, S., 2001a. Carbon isotopic signatures of individual Archean microfossils (?) from Western Australia. Int. Geol. Rev. 43 (3), 196–212.
Ueno, Y., Maruyama, S., Isozaki, Y., Yurimoto, H., 2001b. Early Archean (ca. 3.5 Ga) microfossils and 13C-depleted carbonaceous matter in the North Pole area, Western Australia: Field occurrence and geochemistry. In: Nakashima, S., Maruyama, S., Brack, A., Windley, B.F. (Eds.), Geochemistry and the Origin of Life. Universal Academy Press, Tokyo, pp. 203–236.

Ueno, Y., Yoshioka, H., Maruyama, S., Isozaki, Y., 2004. Carbon isotopes and petrography of kerogens in~ 3.5-Ga hydrothermal silica dikes in the North Pole area, Western Australia. Geochim. Cosmochim. Acta 68 (3), 573–589.
Ueno, Y., Yamada, K., Yoshida, N., Maruyama, S., Isozaki, Y., 2006. Evidence from fluid inclusions for microbial methanogenesis in the early Archaean era. Nature 440 (7083), 516–519.
Uysal, I.T., et al., 2011. Trace element composition of near-surface silica deposits—a powerful tool for detecting hydrothermal mineral and energy resources. Chem. Geol. 280 (1–2), 154–169.
Van Kranendonk, M.J., 2000. Geology of the North Shaw 1: 100 000 Sheets: Sheets 2755. Geological Survey of Western Australia.
Van Kranendonk, M.J., 2006. Volcanic degassing, hydrothermal circulation and the flourishing of early life on Earth: a review of the evidence from c. 3490-3240 Ma rocks of the Pilbara Supergroup, Pilbara Craton, Western Australia. Earth Sci. Rev. 74 (3), 197–240.
Van Kranendonk, M.J., 2011. Morphology as an indicator of biogenicity for 3.5–3.2 Ga fossil stromatolites from the Pilbara Craton, Western Australia. In: Reitner, J., Quéric, N.-V., Arp, G. (Eds.), Advances in Stromatolite Geobiology. Springer, pp. 537–554.
Van Kranendonk, M.J., Pirajno, F., 2004. Geochemistry of metabasalts and hydrothermal alteration zones associated with c. 3.45 Ga chert and barite deposits: implications for the geological setting of the Warrawoona Group, Pilbara Craton, Australia. Geochem.: Explor. Environ. Anal. 4 (3), 253–278.
Van Kranendonk, M.J., Hickman, A.H., Smithies, R.H., Nelson, D.R., Pike, G., 2002. Geology and tectonic evolution of the archean North Pilbara terrain, Pilbara Craton, Western Australia. Econ. Geol. 97 (4), 695–732.
Van Kranendonk, M.J., Webb, G.E., Kamber, B.S., 2003. Geological and trace element evidence for a marine sedimentary environment of deposition and biogenicity of 3.45 Ga stromatolitic carbonates in the Pilbara Craton, and support for a reducing Archaean Ocean. Geobiology 1 (2), 91–108.
Van Kranendonk, M.J., Hugh Smithies, R., Hickman, A.H., Champion, D., 2007. Review: secular tectonic evolution of Archean continental crust: interplay between horizontal and vertical processes in the formation of the Pilbara Craton, Australia. Terra Nova 19 (1), 1–38.
Van Kranendonk, M.J., Philippot, P., Lepot, K., Bodorkos, S., Pirajno, F., 2008. Geological setting of Earth's oldest fossils in the ca. 3.5 Ga Dresser Formation, Pilbara Craton, Western Australia. Precambrian Res. 167 (1), 93–124.
Van Kranendonk, M.J., et al., 2019. Depositional setting of the Fossiliferous, c. 3480 Ma Dresser Formation, Pilbara Craton: A Review. In: Van Kranendonk, M.J., Bennett, V., Hoffmann, E. (Eds.), In: Earth's Oldest Rocks. Elsevier, pp. 985–1006.
Van Kranendonk, M.J., et al., 2021a. Elements for the origin of life on land: a deep-time perspective from the Pilbara Craton of Western Australia. Astrobiology 21 (1), 39–59.
Van Kranendonk, M.J., et al., 2021b. Life analog sites for Mars from early Earth: diverse habitats from the Pilbara Craton and Mount Bruce Supergroup, Western Australia. In: Mars Geological Enigmas. Elsevier, pp. 357–403.
van Zuilen, M.A., 2019. The Significance of Carbonaceous Matter to Understanding Life Processes on Early Earth. In: Van Kranendonk, M.J., Bennett, V., Hoffmann, E. (Eds.), Earth's Oldest Rocks, 2nd ed. Elsevier, pp. 945–984.
Wacey, D., Noffke, N., Cliff, J., Barley, M.E., Farquhar, J., 2015. Micro-scale quadruple sulfur isotope analysis of pyrite from the~ 3480 Ma Dresser Formation: New insights into sulfur cycling on the early Earth. Precambrian Res. 258, 24–35.
Wacey, D., Noffke, N., Saunders, M., Guagliardo, P., Pyle, D., 2018. Volcanogenic pseudo-fossils from the~ 3.48 Ga Dresser Formation, Pilbara, Western Australia. Astrobiology 18, 539–555.
Walter, M.R., 1976. Stromatolites: Developments in Sedimentology, 20. Elsevier, Amsterdam.
Walter, M.R., Buick, R., Dunlop, J.S.R., 1980. Stromatolites 3,400–3,500 Myr old from the North Pole area, Western Australia. Nature 284, 443–445.
Webb, G.E., Kamber, B.S., 2000. Rare earth elements in Holocene reefal microbialites: a new shallow seawater proxy. Geochim. Cosmochim. Acta 64 (9), 1557–1565.
White, D.E., Thompson, G.A., Sandberg, C.H., 1964. Rocks, structure, and geologic history of Steamboat Springs thermal area, Washoe County, Nevada. US Geol. Surv. Prof. Pap. 458-B, 63.
Wilson, C.J., Rowland, J.V., 2016. The volcanic, magmatic and tectonic setting of the Taupo Volcanic Zone, New Zealand, reviewed from a geothermal perspective. Geothermics 59 (Part B), 168–187.
Wood, S.A., 2006. Rare earth element systematics of acidic geothermal waters from the Taupo Volcanic Zone, New Zealand. J. Geochem. Explor. 89 (1–3), 424–427.